Experimental and Analytical Investigation of a Dynamic Gas Squeeze Film Bearing including Asperity Contact Effects

Except where reference is made to the work of others, the work described in this thesis is my own or was done in collaboration with my advisory committee. This thesis does not include proprietary or classified information.

Manoj Deepak Mahajan

Certificate of Approval:

George T. Flowers
Professor
Mechanical Engineering

Robert L. Jackson, Chair
Assistant Professor
Mechanical Engineering

Jay M. Khodadadi
Professor
Mechanical Engineering

Joe F. Pittman
Interim Dean
Graduate School

Experimental and Analytical Investigation of a Dynamic Gas Squeeze Film Bearing including Asperity Contact Effects

Manoj Deepak Mahajan

A Thesis

Submitted to

the Graduate Faculty of

Auburn University

in Partial Fulfillment of the

Requirements for the

Degree of

Master of Science

Auburn, Alabama
December 15, 2006

Experimental and Analytical Investigation of a Dynamic Gas Squeeze Film Bearing including Asperity Contact Effects

Manoj Deepak Mahajan

Permission is granted to Auburn University to make copies of this thesis at its discretion, upon the request of individuals or institutions and at their expense. The author reserves all publication rights.

_____

Signature of Author

_____

Date of Graduation

Vita

Manoj Mahajan, son of Deepak and Neeta Mahajan was born on January 19, 1981, in Nasik District in India. He attended Government College of Engineering, Pune and graduated in November 2002 with the degree of Bachelor of Engineering in Mechanical Engineering. He joined the Masters program in the department of Mechanical Engineering at Auburn University in August 2004.

Thesis Abstract

Experimental and Analytical Investigation of a Dynamic Gas Squeeze Film Bearing including Asperity Contact Effects

Manoj Deepak Mahajan

Master of Science, December 15, 2006
(B.E., Government College of Engineering, Pune University, 2002)

123 Typed Pages

Directed by Robert L. Jackson

This thesis presents a theoretical and an experimental investigation of planar gas squeeze film bearings. The thickness and pressure profile of the gas squeeze film are obtained by simultaneously solving the Reynolds equation and the equation of motion for the squeeze film bearing. This work also accounts for the force due to surface asperity contact in the equation of motion. When the surfaces are in contact, the model predicts the contact force as a function of film thickness. Computational simulations are performed to study the development of the squeeze film from its initial state to a pseudo-steady state condition and to evaluate its load carrying capacity. For certain cases, the simulation results correlate well with the pre-established analytical results. However, corrections must be made to the analytical equations when they are used out of their effective range. In the experimental study, a squeeze film is developed due to an applied relative normal motion between two

parallel circular plates of which one circular plate is effectively levitated. Theoretical results for the squeeze film thickness match qualitatively with its experimental counterpart.

On successful testing of macro-scale gas squeeze film bearings, micro-scale bearing surfaces are fabricated. Experimental investigation of micro-scale bearings suggests that these bearings have significant potential for a wide range of applications in Micro-Electro Mechanical Systems (MEMS).

Acknowledgments

I wish to thank my advisor, Dr. Robert L. Jackson, for providing me with an opportunity to conduct research in the exciting field of tribology. His guidance, support and encouragement have helped me towards the successful completion of my Master's Degree in Engineering. He is a great mentor and working with him was a wonderful experience. I would like to extend my appreciation and thanks to Dr George Flowers for all the help with the test setup and being part of my graduate committee. I would also like to thank Dr. Jay Khodadadi for serving as a graduate committee member.

Many thanks to Klaus Hornig, Dr. Roland Horvath and Alfonso Moreira for their help and motivation at the Vibration Analysis Laboratory. Special thanks to Mr. Charles Ellis and Abhishek for all the help at Alabama Microelectronics Science and Technology Center. I wish to acknowledge my companions here at Auburn, Harish, Rajendra, Harshavardhan, Ananth and Ravi Shankar for their friendship.

I wish to dedicate this work to my parents and sisters for their enduring love, immense moral support and encouragement in the journey of life.

Style manual or journal used LATEX: A Document Preparation System by Leslie Lamport (together with the style known as "aums") and Bibliography as per Tribology Transactions

Computer software used TEX (specifically LATEX), MATLAB 7.0.4, MS Office PowerPoint 2003 and the departmental style-file aums.sty

Table of Contents

List of Figures xi

List of Tables xiii

Nomenclature xiv

1 Introduction 1

2 Background 3
2.1 Introduction . . . 3
2.2 Lubrication . . . 3
2.3 Squeeze Film Effect . . . 5
2.4 Incompressible Squeeze Film Bearings . . . 6
2.5 Compressible Squeeze Film Bearings . . . 7
2.6 Squeeze Film Damping . . . 13
2.7 Micro-Scale Squeeze Film Bearings and Effects Due to Molecular Dynamics 18

3 Objectives 24

4 Numerical Investigation 26
4.1 Introduction . . . 26
4.2 Thin Squeeze Film Bearings . . . 26
4.2.1 Formulation of Coupled Dynamics . . . 26
4.2.2 Computational Scheme . . . 33
4.2.3 Results . . . 38
4.3 Ultra-Thin Squeeze Film Bearings . . . 47
4.3.1 Formulation of Coupled Dynamics . . . 47
4.3.2 Solution Methodology . . . 48
4.3.3 Results . . . 48

5 Experimental Investigation 50
5.1 Thin Squeeze Film Bearings . . . 50
5.1.1 Experimental Setup . . . 50
5.1.2 Experimental Results . . . 57
5.2 Ultra-thin Squeeze Film Bearings . . . 63
5.2.1 Design of Micro-Scale Bearing Surfaces . . . 63
5.2.2 Fabrication of Micro-Scale Bearing Surfaces . . . 65
5.2.3 Results . . . 69

6 Summary 73

Bibliography 75

Appendices 79

A Contact Force 80

B C-program to solve the coupled dynamics for thin squeeze films 86

C Tables of Experimental and Simulation Results 93
C.1 Configuration 1 93
C.2 Configuration 2 94
C.3 Configuration 3 96

D Calibration of Capacitance Sensor 98

E Computer program to solve the dynamics for ultra-thin squeeze films 102

List of Figures

2.1 Classification of lubrication 4

2.2 The squeeze film thickness, h, as a function of normalized time, T, (h=h_m(1+ϵ·cos(ωt) and ϵ=$\delta h/h_m$) 9

2.3 Analogy of a squeeze film as a spring-damper system 14

4.1 Schematic of a planar squeeze film bearing 27

4.2 Scheme for discretization of i-spatial variable and j-time variable 28

4.3 Free body diagram of a squeeze film bearing (one degree of freedom) 30

4.4 Algorithm for computational simulation 34

4.5 Dimensionless P as a function of normalized T at R=0.5, σ=1000 and H=1-0.5·sin(T) (16 nodes) 36

4.6 Dimensionless P as a function of normalized T at R=0.5, σ=1000 and H=1-0.5·sin(T) (160 nodes) 36

4.7 Variation in film height for different time steps 37

4.8 Dynamic behavior of the squeeze film height for given input conditions as a function of time 39

4.9 Comparison of the dimensionless squeeze film force, $F(T)/(\pi \cdot {R_0}^2 \cdot p_{atm})$, as a function of normalized time, T, from the numerical simulation and from Langlois squeeze film force model [8] 40

4.10 Change in percentage error between F_i from the numerical simulation and F_n as predicted by Salbu's Eq. as a function of the squeeze number, σ . . . 43

4.11 The results of numerical parametric study for h_m as a function of F_i at a constant frequency 45

4.12 The results of numerical parametric study for h_m as a function of ω 46

4.13 Algorithm for computational simulation of the ultra-thin squeeze film bearing 49

5.1 Schematic explaining the experimental setup 50

5.2 Test stand used for experimental investigation 51

5.3 Disks used for levitation 52

5.4 Photograph illustrates the experimental setup with the capacitance sensor . 53

5.5 Electrical circuit for capacitance measurement 54

5.6 Photograph illustrates the experimental setup with the laser displacement measurement system 55

5.7 Plot of DC voltage from the laser beam displacement measurement system 56

5.8 Experimental and simulation results for the squeeze film height against the amplitude of vibration for bearing configuration 1 (Capacitance measurement system) 58

5.9 Experimental and simulation results for the squeeze film height against the amplitude of vibration for bearing configuration 2 (Laser displacement measurement system) 60

5.10 Experimental and simulation results for the squeeze film height against the amplitude of vibration for bearing configuration 3 (Laser displacement measurement system) 62

5.11 LASICAD drawing of micro bearing surfaces (not to scale and only portions of the textured sections are shown in this enlarged view) 64

5.12 Fabrication procedure for micro-scale bearing surfaces 65

5.13 Schematics of single unit cell (not to scale) 68

5.14 Experimental results of micro-scale bearing 70

5.15 Dimensionless mean pressure, P_n, as a function of normalized time, T, for the ultra-thin squeeze film bearing 71

A.1 Surface profile of a rough bearing surface 83

A.2 Dimensionless contact load as a function of dimensionless mean surface separation 84

List of Tables

2.1 Assumptions and parameters used to estimate the mean free path 20

2.2 Types of flows as per Knudsen number [34] 20

4.1 Comparison of load carrying capacity between F_i in numerical simulation and F_n by Salbu's Eq. 41

5.1 Bearing configurations used for the experimental purpose 51

5.2 Silicon Wafer Cleaning Procedure [42] 66

Nomenclature

English Symbols

A	area of contact (m^2)
B	bearing breadth (m)
bei, ber	Kelvin functions of order zero
bei_1, ber_1	Kelvin functions of order one
C	capacitance (F)
C_{airgap}	capacitance between the squeeze film bearing surfaces (F)
d	gap due to air (m)
E	modulus of elasticity (Pa)
F	squeeze film force (N)
F_i	applied load, i.e. weight of levitating disk (N)
F_d	squeeze film damping force (N)
F_n	mean positive film force (N)
f	frequency (Hz)
G	gas constant ($J{\cdot}K^{-1}{\cdot}mole^{-1}$)
H	dimensionless film thickness, h/h_0
H^*	dimensionless film thickness, h/h_m
h	thickness of squeeze film in z direction (m)

h_0	initial film thickness (m)
h_m	mean film thickness (m)
Kn	Knudsen number
k	dielectric constant for air
m	mass of the levitated plate (kg)
P	dimensionless pressure, p/p_{atm}
p	pressure (Pa)
p_{atm}	atmospheric pressure (Pa)
$\overline{Q}_P$	rarefaction coefficient
R	dimensionless radius, r/R_0
R_0	radius of area of contact (m)
R_q	RMS surface roughness (m)
r	radial coordinate in cylindrical polar coordinates
S_y	yield strength (Pa)
T	normalized time (rad), ωt
T_g	gas temperature (K)
t	time (s)
U_R, U'_R	physical components of surface motion in cylindrical polar coordinates
U_x, U'_x	dimensionless surface velocity components, u_x/V, u'_x/V
U_y, U'_y	dimensionless surface velocity components, u_y/V, u'_y/V
u_x, u'_x	surface velocity components of respective bearing surfaces

	in x-direction ($\mathrm{m{\cdot}s^{-1}}$)
u_y, u'_y	surface velocity components of respective bearing surfaces
	in y-direction ($\mathrm{m{\cdot}s^{-1}}$)
V	reference velocity ($\mathrm{m{\cdot}s^{-1}}$)
V_{in}	input voltage to the capacitance sensor (V)
$V_{o/p}$	output voltage measured across the capacitor (V)
W_n	mean load capacity
X, Y	dimensionless right-handed Cartesian coordinates, x/B, y/B
x, y, z	right-handed Cartesian coordinates (m)
Z_0	amplitude of vibration of base plate (m)
z_b	displacement of base plate (m)
z_t	displacement of top disk (m)

Greek Symbols

ΔR	step-size for R
ΔT	step-size for T (rad)
δh	amplitude of oscillation of squeeze film at a steady state
ϵ	excursion ratio
ϵ_0	permittivity of free space ($\mathrm{F{\cdot}m^{-1}}$)
η	polytropic coefficient
θ	angular coordinate in cylindrical polar coordinates (rad)

Λ	bearing number
λ	mean free path (m)
μ	viscosity (Pa·s)
μ_{eff}	effective viscosity (Pa·s)
ν	Poisson's Ratio
ρ	density (kg·m^{-3})
σ	squeeze number based on initial film height
σ^*	squeeze number based on mean film height
${\phi_X}^P$, ${\phi_Y}^P$	pressure flow factors in x and y direction
ω	angular velocity (rad·s^{-1}), $2\pi f$

Subscripts:

cont	contact between rough surfaces
i	nodal value in radial direction
j	nodal value in time
n	nominal or apparent value

Chapter 1

Introduction

Research in the field of tribology, the science and technology of friction, wear and lubrication, has been continuously improving the performance of mechanical systems ever since the industrial revolution. A British government report (the "Jost Report") in 1966 estimated a potential savings of £ 515 million per annum only for the United Kingdom by better application of tribological principles and practices [1]. Application of principles of tribology led to the development of many different types of bearings used for different purposes. Thrust bearings, hydrodynamic bearings, hydrostatic bearings, rolling element bearings, etc. are widely used as means to reduce the frictional losses in mechanical systems based on the selection criteria. The selection criteria include speed, load, life, maintenance, space requirements and environmental conditions etc.

The largely underutilized squeeze film effect has a potential for use as a means to lubricate surfaces by creating squeeze film bearings. Applications of such squeeze film bearings can be used in read/write heads in hard disk drives, manufacturing processes, vibrating machinery, low-speed applications and hydrodynamic bearing start up and shut down. In this research, the thin gas squeeze film bearings are studied extensively. Both numerical and experimental results confirm that squeeze film bearings can be used as means for lubrication. Micro-scale bearing surfaces are fabricated to study ultra-thin squeeze films for lubrication of miniaturized mechanical systems.

In Chapter 2 of this thesis, a review of the squeeze film effect with the perspective of lubrication and damping is presented. The various lubrication regimes are described. Hydrodynamic lubrication as well as squeeze film lubrication are defined. Physics and fundamentals of the squeeze film effect are explained. Incompressible and compressible squeeze film bearings, with their governing equations, are reviewed. The latter part of chapter 2 gives a background of squeeze film damping. It gives a concise overview of the cut-off frequency, squeeze film damping and spring forces. This is followed by a review of ultra-thin squeeze film bearings where gas rarefaction effects are significant.

In Chapter 3, all the research objectives as well as the specific goals pertaining to these objectives are stated.

Chapter 4 is divided into two sections, namely Thin and Ultra-thin squeeze film bearings. Each section covers subsections such as formulation of coupled dynamics (the equation of motion and the Reynolds equation for the bearing), numerical scheme to solve the dynamics, followed by the results of the numerical investigation.

Chapter 5 explains all the observations made during the measurements of thin and ultra-thin squeeze film bearings. Here, experimental results are compared with the simulation results.

Chapter 6 summarizes the thesis. In summary, a thorough study was conducted on the squeeze film bearings for their use as a potential means to lubricate surfaces.

Chapter 2

Background

2.1 Introduction

This chapter discusses in detail the different types of lubrication regimes. The phenomenon of squeeze film effect with the perspective of lubrication is then described. Incompressible and compressible squeeze film bearings with their governing equations are reviewed. Then, the squeeze film damping phenomenon and its cut-off frequency are explained. Lastly, ultra-thin (nano-scale) squeeze film bearings including effects due to molecular dynamics are studied.

2.2 Lubrication

"Lubrication is an application of a lubricant between two surfaces in relative motion for the purpose of reducing friction and wear or other forms of surface deterioration" [2]. The lubricant is usually a fluid, but in some cases it can be a solid such as a powder. Lubrication is broadly classified into fluid-film, boundary and mixed regimes (see Fig. 2.1). In fluid-film lubrication, bearing surfaces are completely separated by either a liquid or a gaseous lubricating film [3]. If the loads are high or speeds are low then the contact between high or tall asperities is likely to occur. This is a boundary lubrication regime where a suitable molecular layer of lubricant covers the high asperities. Hence, metal welding due to adhesion

is avoided [3]. The lubrication regime between boundary and fluid-film is categorized as mixed or partial lubrication. In the mixed lubrication regime, effects due to both, boundary and fluid-film lubrication are observed [3]. In fluid-film lubrication, a thin fluid film between

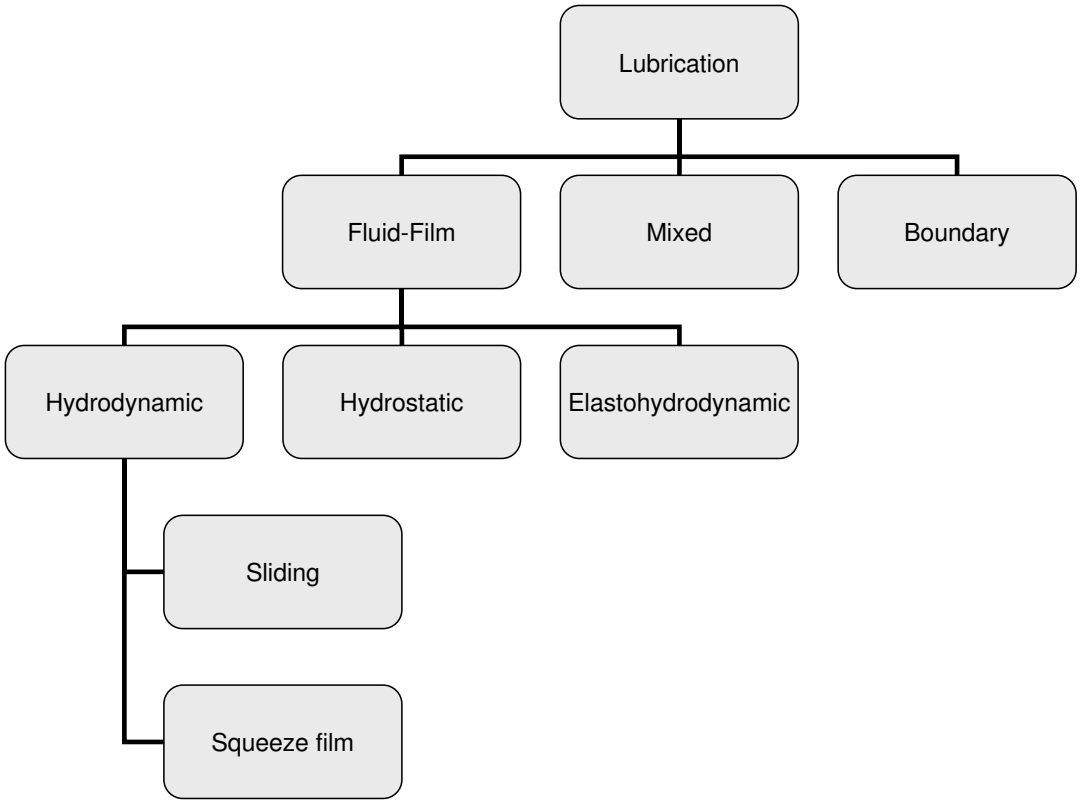

Figure 2.1: Classification of lubrication

bearing surfaces is obtained by either hydrostatic or hydrodynamic action. Hydrostatic lubrication is a phenomenon of maintaining a lubricating film by external means; whereas, hydrodynamic lubrication is self-acting. In hydrodynamic lubrication, positive film pressure between conformal surfaces is developed due to relative motion and fluid viscosity [3]. The topic of interest here is squeeze film lubrication, which is a type of hydrodynamic lubrication

where a lubricating film is developed due to relative normal motion and fluid viscosity. Elastohydrodynamic lubrication is a form of hydrodynamic lubrication where lubricating surfaces are elastically deformable [3].

2.3 Squeeze Film Effect

The term "squeeze film" defines a fluid film contained between two conformal, moving surfaces with velocities of the surfaces normal to the planes of the containment [4]. If the bearing surfaces approach each other then the motion is termed as "positive squeeze". Conversely, if the bearing surfaces move apart then the motion is termed as "negative squeeze" [4]. A relative normal motion between two parallel surfaces can produce a squeeze film which can completely separate the surfaces and contribute to lubrication. This phenomenon is known as the "squeeze film effect" [3].

The load-carrying capacity results from the fact that a viscous flow cannot be squeezed out of the gap without any delay; therefore, providing a cushioning effect and the film equilibrium is established through a balance between viscous flow forces and compressibility effects [5]. Thus, the flow of fluid at the boundary is approximately reduced to zero due to high viscous forces resulting from alternate compression and decompression of the fluid [6]. Alternate compression and decompression produces a steady-state film pressure which oscillates about its mean value [6]. The average steady-state film pressure is greater than the atmospheric pressure over one cycle (T to $T+2\pi$) and thus provides the squeeze film lift and lubrication [6]. Applications of the squeeze film effect are clutch packs in automotive

transmission, engine piston pin bearings, human hip and knee joints, damper films for jet engine ball bearings and piston rings [7].

The dynamics of squeeze film is coupled as it includes both the equation of motion for squeeze film bearing and the Reynolds equation. Here, the Reynolds equation governs the generated fluid pressure. The general form of the Reynolds equation is given by [3]

$$\frac{\partial}{\partial x}\left(\frac{\rho h^3}{12\mu}\frac{\partial p}{\partial x}\right)+\frac{\partial}{\partial y}\left(\frac{\rho h^3}{12\mu}\frac{\partial p}{\partial y}\right)=\frac{\partial}{\partial x}\left(\frac{\rho h\left(u_x+u_x'\right)}{2}\right)+\frac{\partial}{\partial y}\left(\frac{\rho h\left(u_y+u_y'\right)}{2}\right)+\frac{\partial(\rho h)}{\partial t} \tag{2.1}$$

Here, h is the squeeze film height and μ is the viscosity of the fluid. The time dependent term $\frac{\partial(\rho h)}{\partial t}$ is known as the "squeeze term" as it represents squeezing motion of the fluid. Here, u_x, u_y and u_x', u_y' are surface velocity components of bottom and top surfaces in x and y direction, respectively.

2.4 Incompressible Squeeze Film Bearings

In incompressible squeeze film bearings, the lubricant is a liquid and its density is assumed to be constant in the operating range. As per Hamrock [3], when two surfaces approach each other, it takes a finite amount of time to squeeze out the fluid, and this action provides a lubricating effect. It is also interesting to note that it takes an infinite amount of time to theoretically squeeze out all the fluid. For an incompressible fluid, viscosity along with density is assumed to be constant in the Reynolds equation [3]. Also, if

only normal motion is considered and sliding velocities are zero then the Reynolds equation in rectangular coordinates is given as [3]

$$\frac{\partial}{\partial x}\left(h^3\frac{\partial p}{\partial x}\right)+\frac{\partial}{\partial y}\left(h^3\frac{\partial p}{\partial y}\right)=12\mu\frac{\partial h}{\partial t} \tag{2.2}$$

Eq. (2.2) in cylindrical-polar coordinates is expressed as

$$\frac{\partial}{\partial r}\left(rh^3\frac{\partial p}{\partial r}\right)+\frac{1}{r}\frac{\partial}{\partial \theta}\left(h^3\frac{\partial p}{\partial \theta}\right)=12\mu r\frac{\partial h}{\partial t} \tag{2.3}$$

The Reynolds equation given in the form of Eqs. (2.2) and (2.3) can be analytically solved for pressure, film thickness and finite squeeze time (i.e. the amount of time for the film to be squeezed out). Hamrock [3] provides analytical expressions for pressure, film thickness and finite squeeze time for various geometries such as parallel-surface bearings with infinite width, journal bearings with no rotation, a parallel circular plate approaching a plane surface and a long cylinder near plane. As per Hamrock [3], the parallel film shape produces the largest normal load-carrying capacity.

2.5 Compressible Squeeze Film Bearings

In contrast, for compressible squeeze film bearings, the lubricant used is gaseous (such as ambient air). Langlois [8] was one of the first to extensively study the isothermal gas

squeeze films with the assumption of a thin and continuous gas film with a constant viscosity. Langlois [8] also assumed that the density of the gas is proportional to the pressure, which means that the gas squeeze film obeys the ideal gas law under isothermal conditions. Langlois [8] derived the equation that governs the pressure variation for a thin, flat isothermal gas squeeze film

$$\frac{\partial}{\partial X}\left(H^3 P\frac{\partial P}{\partial X}\right)+\frac{\partial}{\partial Y}\left(H^3 P\frac{\partial P}{\partial Y}\right)=\Lambda\left(\frac{\partial}{\partial X}\left[PH\left(U_x+U_x'\right)\right]\right) +\Lambda\left(\frac{\partial}{\partial Y}\left[PH\left(U_y+U_y'\right)\right]\right)+\sigma\frac{\partial PH}{\partial T} \tag{2.4}$$

Here, Λ is the bearing number and σ is the squeeze number.

The definitions of Λ and σ are

$$\Lambda = 6\mu BV/p_{atm}{h_0}^2 \tag{2.5}$$

$$\sigma = 12\mu B^2\omega/p_{atm}{h_0}^2 \tag{2.6}$$

Here, B is bearing breadth. The reference velocity, V, is used to obtain normalized U_x, U_x', U_y and U_y' (see Nomenclature), where the order of magnitude of these normalized velocities is unity [8]. Likewise, Eq. (2.4) in cylindrical-polar coordinates is given as

$$\frac{\partial}{\partial R}\left(RH^3P\frac{\partial P}{\partial R}\right)+\frac{1}{R}\frac{\partial}{\partial\Theta}\left(H^3P\frac{\partial P}{\partial\Theta}\right)=\Lambda\left\{\frac{\partial}{\partial R}\left[RPH\left(U_R+U_R'\right)\right]\right\}$$
$$+\Lambda\left\{\frac{\partial}{\partial\Theta}\left[PH\left(U_\Theta+U_\Theta'\right)\right]\right\}+R\sigma\frac{\partial(PH)}{\partial T} \tag{2.7}$$

Later, Langlois [8] dealt with the exact solution to squeeze film equations (Eqs. (2.4) and

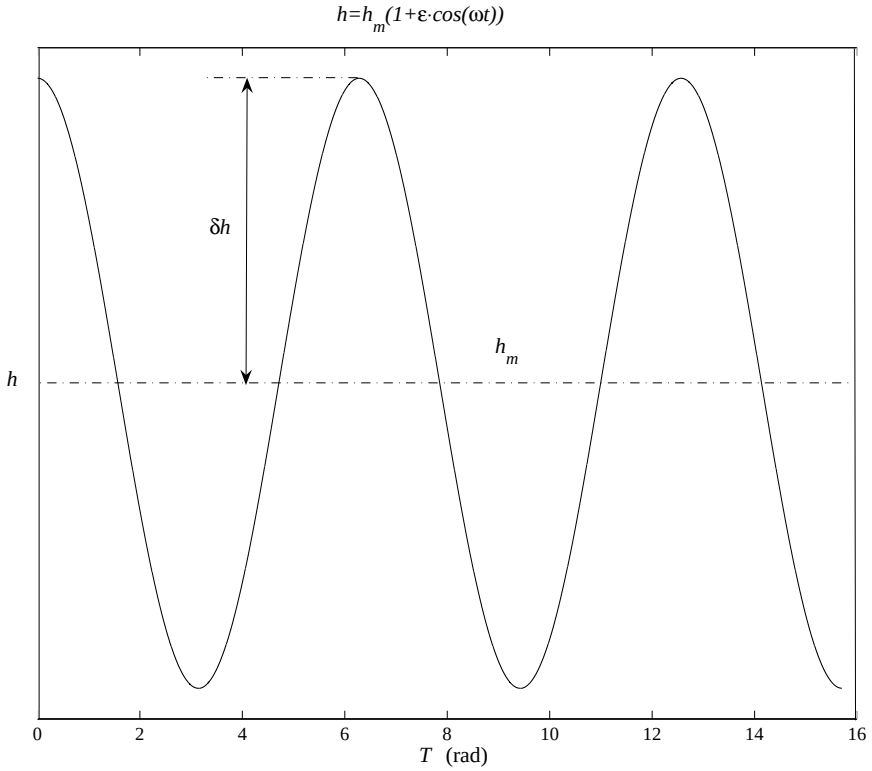

Figure 2.2: The squeeze film thickness, h, as a function of normalized time, T, (h=h_m(1+ϵ·cos(ωt) and ϵ=$\delta h/h_m$)

(2.7)) by assuming the squeeze film thickness as a function of time (see Fig. 2.2)

$$h = h_m \left(1 + \epsilon \cdot \cos \omega t\right) \tag{2.8}$$

Based on the assumption of a film thickness given by Eq. (2.8), Langlois [8] introduced a perturbation parameter for pressure of the order of ϵ in the Reynolds equation. Then, Langlois [8] solved Eq.(2.4) to obtain the squeeze film force (i.e. the force due to the difference between the pressure of the squeeze film and the ambient pressure for a given instant of time). This solution is given for the squeeze film between two flat long parallel plates and two parallel disks. Since the present work considers axisymmetric parallel disks without lateral surface motions, the governing Reynolds equation as per [8] is

$$\frac{\partial}{\partial R}\left(RH^3 P \frac{\partial P}{\partial R}\right) = R\sigma \frac{\partial (PH)}{\partial T} \tag{2.9}$$

where σ is as given

$$\sigma = 12\mu {R_0}^2 \omega / p_{atm} {h_m}^2 \tag{2.10}$$

As per [8], if the squeeze number is very large then the gas between bearing surfaces does not leak, and the squeeze film can be considered as incompressible. At low squeeze

numbers, the frequency of squeeze motion is low, and therefore gas leaks out [8]. The squeeze film force between parallel disks given by [8] is

$$F(T) = \left(\pi p_{atm} {R_0}^2 \epsilon\right) \left[-g_1(\sigma)\cos T + g_2(\sigma)\sin T\right] \tag{2.11}$$

where,

$$g_1(\sigma) = 1 - \sqrt{\frac{2}{\sigma}} \cdot \frac{ber\sqrt{\sigma}\left(bei_1\sqrt{\sigma} - ber_1\sqrt{\sigma}\right) - bei\sqrt{\sigma}\left(ber_1\sqrt{\sigma} + bei_1\sqrt{\sigma}\right)}{\left(ber\sqrt{\sigma}\right)^2 + \left(bei\sqrt{\sigma}\right)^2} \tag{2.12}$$

$$g_2(\sigma) = \sqrt{\frac{2}{\sigma}} \cdot \frac{ber\sqrt{\sigma}\left(ber_1\sqrt{\sigma} + bei_1\sqrt{\sigma}\right) + bei\sqrt{\sigma}\left(bei_1\sqrt{\sigma} - ber_1\sqrt{\sigma}\right)}{\left(ber\sqrt{\sigma}\right)^2 + \left(bei\sqrt{\sigma}\right)^2} \tag{2.13}$$

Eq.(2.11) gives a good estimate of the squeeze film force between parallel disks at a particular instant of time.

For compressible squeeze film bearings, Salbu [9] showed that the squeeze film effect can be used to operate bearings in a highly vibrational environment, and also provided analytical equations for bearing load carrying capacity. Salbu [9] assumes that the squeeze film thickness is a known sinusoidal function of time. One disk is held stationary and the other oscillates sinusoidally about a mean film thickness in a direction normal to the surfaces with an amplitude of oscillation, δh, and frequency, ω. Salbu [9] uses a simplified

form of the Reynolds equation (Eq.(2.9)). Then, the boundary conditions for the planar radial squeeze film bearing are assumed as

$$P\,(R,T=0)=1 \tag{2.14}$$

i.e. initial pressure between disks is atmospheric. At the outer periphery,

$$P\,(R=1,T)=1 \tag{2.15}$$

i.e. the pressure is atmospheric at all times. At equilibrium, the mean positive film force, is equal to the applied load. When $\sigma\rightarrow\infty$, "the mass content rule" can be imposed on Eq. (2.9) and the following equation can be derived to approximate the mean load carrying capacity [9]

$$W_n=\frac{F_n}{\pi p_{atm}{R_0}^2}=\left\{\left[\frac{1+\frac{3}{2}\epsilon^2}{1-\epsilon^2}\right]^{1/2}-1\right\} \tag{2.16}$$

Salbu [9] numerically modeled W_n as a function of σ for various ϵ values and compared it with the asymptotic values of W_n, as given by Eq. (2.16). For $\sigma\geq10$, Salbu [9] observed little variation between the numerical and analytical W_n predicted from Eq. (2.16) at the same ϵ. Thus, Eq. (2.16) may be used to predict W_n for $\sigma\geq10$. For $\sigma\geq10$, Eq.(2.16) is

used to validate the computational simulation results of the current analysis presented in this thesis and will be referred to as Salbu's Equation.

Further work on dynamic gas squeeze film bearing theory was performed by Minikes et al. [10]. In [10], instead of assuming a squeeze film height as a function of time, it is determined by equilibrium of forces. Minikes et al. [10] used a piezoelectrically vibrating disk to levitate another disk for experimental and numerical work. A sinusoidal voltage was applied on the electrodes which gave rise to harmonic deformation of the piezoelectric disk at the excitation frequency. The piezoelectric disk was also statically and dynamically deforming. However, in the present work both disks are considered to be rigid. A similar approach of coupled dynamics can also be found in [11], where the fluid film lubrication forces and seal dynamics were solved simultaneously for noncontacting gas face seals, although the faces were annular and not circular.

2.6 Squeeze Film Damping

"Damping is the element, present in all real systems, which dissipates vibrational energy, usually as heat, and so attenuates the motion" [12]. A squeeze film can also be modeled as a spring-damper system (Fig. 2.3).

An early study of squeeze film by Griffin et al. [13] suggests that squeeze film between two parallel plates provides viscous damping action over a certain frequency range. As per Griffin et al. [13], if the displacements to be damped are small (sub micrometer) then squeezing of a thin gas film between two parallel flat surfaces can produce substantial

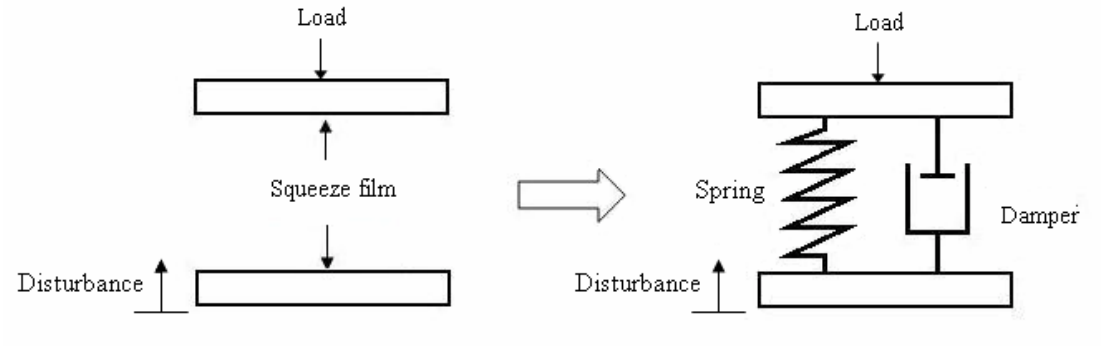

Figure 2.3: Analogy of a squeeze film as a spring-damper system

damping forces at very high frequencies. The damping force is proportional to the relative velocity over certain ranges of operation, and this type of damper is termed a viscous damper [13]. Squeeze film damping due to relative axial or tilting motion between two closely spaced plates is analyzed by Griffin et al. [13]. Griffin et al. [13] provides a critical frequency below which the squeeze film acts as a damper and above which it acts as a spring. At the critical frequency, both the damping and spring forces are equal. Analytical expressions are also provided by Griffin et al. [13] for the squeeze film force and critical frequency for special cases of infinitely wide parallel plates, annular parallel plates and parallel disks. The critical frequency for parallel disks is given by [13]

$$\omega_c = \frac{\eta {h_m}^2 p_a}{2.07 \mu {R_0}^2} \tag{2.17}$$

Blech [14] also analyzed squeeze film cut-off frequencies for different geometries and divided the squeeze film force into damping and spring force components. The spring force

is greater than the damping force for all frequencies except the cut-off frequency, and below the cut-off frequency damping is comparable to spring action [14]. As per Blech [14], the maximum damping occurs at the cut-off frequency when the spring and damping forces are equal, and above the cut-off frequency, the spring force increases while the damping force decreases with increases in the squeeze number, σ.

Blech [14] gives the damping force as a function of the squeeze number, σ, and excursion ratio, ϵ, between parallel circular disks

$$F_d = -\sqrt{\frac{2}{\sigma}} \cdot \left[A_c \left(ber_1\sqrt{\sigma} - bei_1\sqrt{\sigma}\right) + B_c \left(ber_1\sqrt{\sigma} + bei_1\sqrt{\sigma}\right)\right] \epsilon \tag{2.18}$$

Similarly, the spring force by [14] is

$$F_s = 1 + \sqrt{\frac{2}{\sigma}} \cdot \left[A_c \left(ber_1\sqrt{\sigma} + bei_1\sqrt{\sigma}\right) + B_c \left(ber_1\sqrt{\sigma} - bei_1\sqrt{\sigma}\right)\right] \epsilon \tag{2.19}$$

Here,

$$A_c = \frac{bei\sqrt{\sigma}}{\left(ber^2\sqrt{\sigma} + bei^2\sqrt{\sigma}\right)} \tag{2.20}$$

and

$$B_c = -\frac{ber\sqrt{\sigma}}{\left(ber^2\sqrt{\sigma} + bei^2\sqrt{\sigma}\right)} \tag{2.21}$$

The critical frequency for parallel disks is given by [14] as

$$\omega_c = \frac{{h_m}^2 p_a}{1.93\mu {R_0}^2} \tag{2.22}$$

For isothermal conditions, Blech [14] (Eq. (2.22)) underestimates the cut-off frequency by 7 % as compared to Griffin et al. [13] (Eq. (2.17)) because Blech [14] assumes one term approximation to the cut-off frequency. A sample cut-off frequency using Eq. (2.17) [13] and assumption of isothermal flow for an experimental result is calculated to be 1377 Hz. For this case (See Apendix C.2), h_m is 13.38 μm and the frequency of oscillation is 800 Hz. Thus, the frequency at which the bearing is operated is less than the cut-off frequency where the spring force is more than the damping force [14]. Similarly, a few more calculations based on the experimental results suggest that in the present work the range of operation of the squeeze film bearing is either below or above the cut-off frequency, and for such cases the spring force is always greater than the damping force [14].

The gas squeeze film stiffness and damping torques on a circular disk oscillating about its diameter were analyzed by Ausman [15]. In [15], the linearized Reynolds equation for small squeeze film motions is solved for pressure between the disks where one disk oscillates in a tilting motion about its diameter. This pressure is then integrated over the surface

area to obtain the total squeeze film torque. Then Ausman [15] separates the total squeeze film torque into stiffness and damping components. As per Ausman [15], the torque which opposes the angular deflection is stiffness torque; whereas, the torque which opposes angular rate is damping torque. The gas damping is observed as viscous friction of the gas as it flows in and out between the disks, and gas stiffness is observed as compressibility of a trapped gas between the disks [15]. Ausman[15] concludes that at higher frequencies, the gas is trapped and does not leak, resulting in higher compressibility. This means that higher frequencies produce higher stiffness torque, and at lower frequencies, gas has more than sufficient time to flow in and out, resulting in higher damping torque[15].

Etsion [16] analyzed squeeze film effects in liquid lubricated radial face seals and obtained damping coefficients. Green et al. [17] calculated dynamic damping and stiffness coefficients of the fluid films in mechanical face seals, considering squeeze film effects along with hydrostatic and hydrodynamic effects. Work specific to compressible squeeze film damping was done by Blech [18] for annular squeeze-film plates in relative motion. Research into the effect of squeeze film damping is also currently prominent in the design of micro-electro mechanical systems (MEMS) and microstructures ([19]-[26]). Some of this work is discussed in detail in the next section.

2.7 Micro-Scale Squeeze Film Bearings and Effects Due to Molecular Dynamics

Micro-Electro-Mechanical Systems (MEMS) are miniature systems used to combine electro-mechanical functions with dimensions varying from a micrometer to a millimeter. Due to the micrometer size, lubrication in MEMS becomes a critical design parameter and design and selection of MEMS bearings is a challenge for researchers. Usage of liquid lubricant in MEMS leads to a power dissipation problem and so is not a good choice for lubrication [27]. An alternative to oil-based lubricant, gas lubricated bearings can be used in MEMS. Gas bearings can support their loads on pressurized thin gas films. As per Epstein [28], for micromachines such as turbines, gas bearings have several advantages over electromagnetic bearings, such as no temperature limits, high load carrying capability, and relatively simple fabrication. "The relative load-bearing capability of a gas bearing improves as size decreases since the volume-to-surface area ratio (and thus the inertial load) scales inversely with size" [28]. An example of a fully functional gas film bearing is seen in the MIT Microengine project [29]. Here, a rotor of a micro-gas turbine generator is supported by a journal air bearing. As per Breuer [30], the gas lubrication system in MEMS should be easy to fabricate with sufficient performance and robustness. In another example, a self-acting gas thrust bearing was designed, fabricated and tested on a silicon microturbine [31]. Wong et al. [31] compared a hydrodynamic gas thrust bearing to an existing hydrostatic one, and observed that a hydrodynamic approach is much simpler to fabricate and the required source of pressurized gas can be eliminated.

If the high speed relative normal motion is already available in MEMS, then potentially the squeeze film effect can be used as a means to lubricate surfaces in MEMS, and create MEMS bearings. In such cases, there is no special geometry needed as two planar surfaces serve as a bearing, and the system is also maintenance free because ambient air serves as the lubricant. Breuer [30], in a summary on some of the issues of lubrication in MEMS, suggests that fundamental issues of fluids and solid physics such as gas surface interactions, momentum and energy accommodation phenomenon and surface contamination effects are vital parameters for ultra-thin lubrication. For such a small scale, continuum assumptions are not always valid, which can be seen in the following calculations. The RMS roughness, R_q, of MEMS surfaces seems rather smooth. The range of R_q is usually varies from 0.07 to 0.25 nm [32]. For a complete surface separation, film thickness of $10 \cdot R_q$ is a good approximation. Thus, a minimum film thickness of 2.5 nm should provide a full film lubrication. The above calculations show that ultra-thin fluid films can be used in MEMS as a means of lubrication.

The mean free path of a gas is given as [33]

$$\lambda = \frac{16\mu}{5p}\sqrt{\frac{GT_a}{2\pi}} \tag{2.23}$$

The mean free path can be estimated for the normal operating conditions (See Table 2.1) in a squeeze film bearing. Using Eq. (2.23) and the assumptions in Table 2.1, the mean free path, λ, is calculated to be 8.7 nm. The mean free path is used to calculate the Knudsen

Table 2.1: Assumptions and parameters used to estimate the mean free path

Flow	Isothermal
Air Temperature, T_a	293 K
Viscosity of air, μ	$1.82{\cdot}10^{-5}$ N·s/m^2
Pressure, p	101325 N/m^2
Gas Constant, G	8.3144 J·mol^{-1}·K^{-1}

number to further characterize the type of fluid flow. The Knudsen number, Kn is defined as

$$Kn = \frac{\text{Mean free path } (\lambda)}{\text{film height } (h)} \tag{2.24}$$

If the mean free path is very small compared to the characteristic length (i.e. length scale of the problem), then the fluid flow is considered to be in the continuum range. If the mean free path is comparable to the characteristic length then continuum theory of fluid mechanics does not hold well. Typical values of the Knudsen number corresponding to different types of flow are tabulated in Table 2.2. Substituting values of λ=8.7 nm and

Table 2.2: Types of flows as per Knudsen number [34]

Range of Knudsen Number	Type of Flow
$Kn \leq 10^{-3}$	Continuum Flow
$10^{-3} < Kn < 0.1$	Slip Flow
$0.1 < Kn < 10$	Transition Flow
$10 \leq Kn$	Molecular Flow

h=2.5 nm in Eq. (2.24) gives $Kn \approx 3.5$. Thus, the mean free path is not negligible when compared to the film thickness and the flow between bearing surfaces cannot be considered

as a continuum any more. For $Kn \approx 3.5$, the fluid flow falls into the transition flow regime (See Table 2.2).

If the film height is increased to 8 μm then the fluid flow will at most change to slip flow. Hsia et al. [35] experimentally studied gas bearings at ultra low clearances and pointed out that for ultra-thin films (below 0.25 microns), slip-flow theory (effects due to molecular dynamics) needs to be considered when modeling the fluid dynamics. There are various models which provide means to include rarefaction effects due to reduction in the density of gas (i.e. slip flow or transition flow regime) in the Reynolds equation ([24],[33],[36],[38]).

Although most of this work is done for the squeeze film damping, the governing equations generally remain the same and can be used for squeeze film lubrication. Li [36] modeled an ultra-thin gas squeeze film using the modified gas film lubrication (MMGL) equation including coupled roughness and rarefaction effects. A rectangular geometry is considered in this work and a linearized form of MMGL equation [36] is solved.

$$\frac{\partial}{\partial x}\left(\left({\phi_X}^P\right)_0 \frac{\partial P}{\partial x}\right)+\frac{\partial}{\partial y}\left(\left({\phi_Y}^P\right)_0 \frac{\partial P}{\partial y}\right)=\alpha^2\left(\mu\frac{\partial H}{\partial t}+\frac{\partial P}{\partial t}\right) \tag{2.25}$$

Here,

$$\alpha^2 = \frac{12\mu}{\eta {h_m}^2 p_{atm}} \tag{2.26}$$

and ${\phi_X}^P$ and ${\phi_Y}^P$ are pressure flow factors in x and y direction respectively.

Then, Li [36] transforms the linearized MMGL problem to the continuum gas film problem to obtain an analytic solution. Darling et al.[37] provides an analytical equation for the squeeze film force in the form of a complex number. The real part of the complex number is the spring force while the imaginary part is the damping force. In an another work by Pandey et al. [24], surface roughness and rarefaction effects are included in the analysis of squeeze film damping in MEMS. This work [24] accounts for nonlinear effects rather than solving the linearized form of the MMGL equation. An explicit finite difference solution of the nonlinear MMGL equation suggests that rarefaction effects reduce the spring force and the damping force below the cut-off frequency but above the cut-off frequency the spring force reduces but the damping force increases when compared with the linearized solution [24]. Rarefaction effects increase the value of the cut-off frequency and so increase the range of frequency where damping is dominant [24]. Thus, in order to achieve lubrication from the squeeze film effect, it should be better to operate the squeeze film bearings above the cut-off frequency.

Nayfeh et al. [23] modeled flexible microstructures under the effect of squeeze film damping. The form of Reynolds equation used by [23] is

$$\frac{\partial}{\partial x}\left(H^3 P\frac{\partial P}{\partial x}\right)+\frac{\partial}{\partial y}\left(H^3 P\frac{\partial P}{\partial y}\right)=12\mu_{eff}\frac{\partial(PH)}{\partial t} \tag{2.27}$$

Here, the effective viscosity, μ_{eff}, is given by Veijola et al. [38] which accounts for the gas rarefaction effects and is given as

$$\mu_{eff}=\frac{\mu}{1+2Kn+0.2\cdot Kn^{0.788}e^{-Kn/10}} \tag{2.28}$$

Eqs. (2.27) and (2.28) can be easily used for modeling the squeeze film effect for ultra-thin films and therefore the present work models ultra-thin squeeze film effect using Eqs. (2.27) and (2.28) (See Chapter 4).

Chapter 3

Objectives

The objective of this research is to experimentally and analytically study dynamic compressible squeeze film bearings. The squeeze film bearings are hydrodynamic bearings where fluid pressure is generated due to relative normal motion between the bearing surfaces. The dynamic motion of gas squeeze film bearings is governed by fluid flow forces, forces due to motion of both the bearing surfaces and the contact forces due to surface asperities. The lubricant used in studied compressible squeeze film bearings is air or gas. Gas lubricated bearings have certain advantages over the liquid lubricated bearings such as low frictional heat and a greater temperature range [39].

In the first part of this thesis, macro-scale dynamic gas squeeze film bearings having thin squeeze films will be studied. The coupled dynamics of macro-scale gas squeeze film bearings which includes the Reynolds equation for fluid flow, the equation of motion for the squeeze film bearing and the contact force due to initial surface asperity interaction will be formulated. Then, coupled equations will be numerically solved to study the dynamic behavior of gas squeeze films from its initial state to pseudo-steady state. Based on numerical investigation, the load carrying capacity to the squeeze number, σ and the excursion ratio, ϵ will be correlated. A test setup will be built to experimentally generate, control and measure the gas squeeze films between disk shaped surfaces. Experimental and numerical results will be compared.

In the latter part of this thesis, micro-scale dynamic gas squeeze film bearings having ultra-thin squeeze films will be studied. The fluid dynamics for micro-scale dynamic gas squeeze film bearings (ultra-thin) as it changes from macro-scale dynamic gas squeeze film bearings (thin) will be modified, and the changes will be incorporated into the coupled dynamic model. Prototypes of micro-scale squeeze film bearings will be fabricated for the experimental study. Finally, experimental and simulation results will be compared.

Chapter 4

Numerical Investigation

4.1 Introduction

This chapter describes in detail the numerical scheme to solve the coupled dynamic system. The results obtained from the numerical investigation are then discussed. The chapter is divided into two parts, thin squeeze film bearings and ultra-thin squeeze film bearings.

4.2 Thin Squeeze Film Bearings

If the squeeze film is thin enough to operate in the continuum flow regime then the bearing is considered to have a thin squeeze film (as opposed to an ultra-thin squeeze film). This section covers the formulation of the coupled dynamics, the computational scheme and the simulation results.

4.2.1 Formulation of Coupled Dynamics

See Fig. 4.1 for a schematic of the dynamic planar gas squeeze film bearing. The bearing configuration consists of two metal disks. Ideally, these metal disks are subjected to only one degree of freedom (permitting motion only in the vertical direction). The bottom disk is used as an oscillating base and the top disk freely levitates just above the bottom disk. The oscillating base is achieved by mounting on a vibrating shaker. At rest,

the upper disk sits on the top surface of the oscillating base. Once the base is subjected to adequate oscillatory motion, the air squeeze film is generated between the oscillating base and the upper disk.

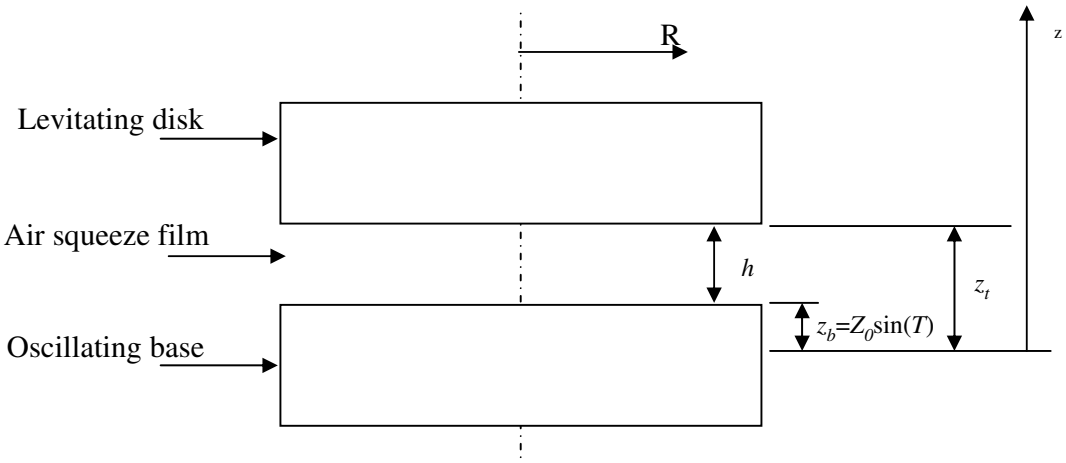

Figure 4.1: Schematic of a planar squeeze film bearing

Assuming that the squeeze film is axisymmetric and isothermal, the normalized Reynolds equation in polar coordinates for an ideal gas between two parallel circular disks is given as

$$\frac{1}{R}\frac{\partial}{\partial R}\left(RH^{*3}P\frac{\partial P}{\partial R}\right) = \sigma^{*}\frac{\partial\left(PH^{*}\right)}{\partial T} \tag{4.1}$$

where the squeeze number, σ^{*}, is as given

$$\sigma^{*} = 12\mu {R_0}^2\omega/p_{atm}{h_0}^2 \tag{4.2}$$

Eq. (4.1) differs from Eq. (2.9) in the manner in which the squeeze film height is normalized. In Eq. (4.1) the squeeze film height, h, is normalized by the initial film height, h_0, whereas in Eq. (2.9) the squeeze film height, h, is normalized by the mean film height, h_m (see nomenclature). The initial film height, h_0, is known; whereas the mean film height, h_m, is unknown before solving the fluid dynamics. Thus, the fluid dynamics is modeled for Eq. (4.1). Eq. (4.1) is a nonlinear parabolic partial differential equation. The boundary conditions of Eq. (4.1) are given by Eqs. (2.14) and (2.15). The initial pressure is ambient and the initial film thickness is determined from a contact force model (see Appendix A). The normalized Reynolds equation (Eq. 4.1) is solved numerically.

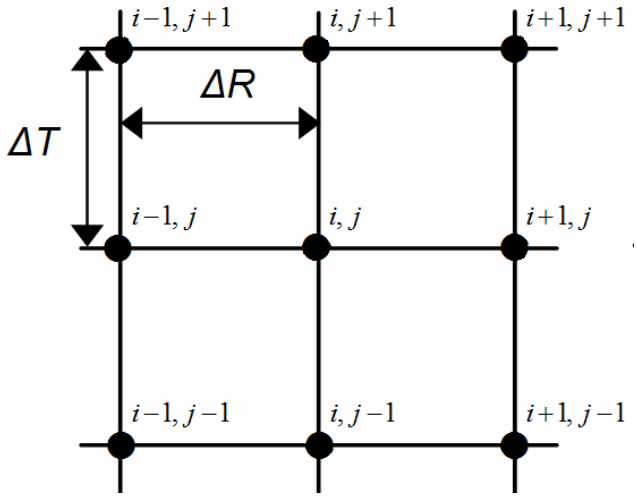

Figure 4.2: Scheme for discretization of i-spatial variable and j-time variable

The left hand side of Eq. (4.1) is discretized using a central-finite difference scheme. Fig. 4.2 explains the meshing scheme for the squeeze film bearing in space (i) and time (j).

For (0<R<1),

$$\frac{1}{R}\frac{\partial}{\partial R}\left[PRH^{*3}\frac{\partial P}{\partial R}\right] \approx \frac{{H^*}_{j+1}^{\,3}}{R_i}\left[R_{i+\frac{1}{2}}P_{i+\frac{1}{2},j+1}\left(\frac{P_{i+1,j+1}-P_{i,j+1}}{\Delta R}\right)\right] - \frac{{H^*}_{j+1}^{\,3}}{R_i}\left[R_{i-\frac{1}{2}}P_{i-\frac{1}{2},j+1}\left(\frac{P_{i,j+1}-P_{i-1,j+1}}{\Delta R}\right)\right] \tag{4.3}$$

where,

$$R_{i+\frac{1}{2}} = \frac{R_i + R_{i+1}}{2} \tag{4.4}$$

$$R_{i-\frac{1}{2}} = \frac{R_i + R_{i-1}}{2} \tag{4.5}$$

$$P_{i-\frac{1}{2},j+1} = \frac{P_{i,j+1} + P_{i-1,j+1}}{2} \tag{4.6}$$

$$P_{i+\frac{1}{2},j+1} = \frac{P_{i,j+1} + P_{i+1,j+1}}{2} \tag{4.7}$$

and at the left boundary (R=0), the pressure gradient $\frac{\partial P}{\partial R}$ is zero.

$$P_{0,j} = P_{0,j+1} \tag{4.8}$$

At the right boundary (R=1), the pressure is always atmospheric.

$$P(R = 1, T) = 1 \tag{4.9}$$

The right hand side of Eq. (4.1) is discretized as

$$\sigma^* \frac{\partial\left(PH^*\right)}{\partial T} \approx \sigma^* \frac{P_{i,j+1}{H^*}_{j+1} - P_{i,j}{H^*}_j}{\Delta T} \tag{4.10}$$

In order to investigate the dynamic squeeze film bearing, it is necessary to consider the coupled dynamics of the system, which includes the Reynolds equation and the equation of motion using a force balance.

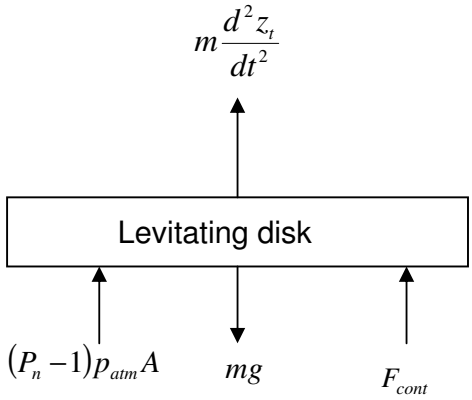

Figure 4.3: Free body diagram of a squeeze film bearing (one degree of freedom)

A free body diagram of the top levitating disk (Fig. 4.3) shows all the forces acting on the top disk. Thus, the equation of motion can be written as

$$m\frac{d^2 z_t}{dt^2} = (P_n - 1) \cdot p_{atm} \cdot A + F_{cont} - F_i \tag{4.11}$$

Here, F_i is the weight of the top disk as employed in the simulation i.e.

$$F_i = mg \tag{4.12}$$

Substituting Eq. (4.12) into Eq. (4.11) gives

$$m\frac{d^2 z_t}{dt^2} = (P_n - 1) \cdot p_{atm} \cdot A + F_{cont} - mg \tag{4.13}$$

Here, the term F_{cont} represents the asperity contact force. The contact force model is presented in the Appendix A. In the equation of motion, contact force between bearing surfaces needs to be considered since the surfaces can be in contact at start-up, shut-down and if the squeeze film force is not large enough to achieve continuous separation of the surfaces. The model detailed in the Appendix A provides an average contact force, F_{cont}, as a function of surface separation or film thickness (h), rms surface roughness (R_q), modulus of elasticity (E), yield strength (S_y) and Poisson's Ratio (ν). Using an exponential fit to the results of Eqs. (A1-A7), an analytical expression of F_{cont} as a function of h is obtained. In the numerical simulation, this relationship is used to predict the contact force between the bearing surfaces. Initially, at $t = 0$, the two surfaces are stationary and the contact force, F_{cont}, balances the applied load, F_i. But during the development of the squeeze film, the two surfaces are pushed out of contact by the reaction force between bearing surfaces. Inclusion of F_{cont} in the dynamics also predicts the initial (at $t = 0$) film thickness h_0 when F_{cont}=mg, and also indicates when a full film of lubrication is achieved (the contact force reaches zero). As the squeeze film thickness, h, is also the relative displacement between the two bearing surfaces (See Fig. 4.1)

$$z_t = z_b + h \tag{4.14}$$

Then taking the time derivative of Eq. (4.14) twice yields

$$\frac{d^2 z_t}{dt^2} = \frac{d^2 z_b}{dt^2} + \frac{d^2 h}{dt^2} \tag{4.15}$$

and since the base is excited by a sine wave

$$z_b = Z_0 \sin T \tag{4.16}$$

Differentiating Eq. (4.16) twice with respect to t yields

$$\frac{d^2 z_b}{dt^2} = -\omega^2 Z_0 \sin T \tag{4.17}$$

Substituting Eqs. (4.15) and (4.17) into Eq. (4.13) yields

$$m\frac{d^2 h}{dt^2} = m\omega^2 Z_0 \sin T + (P_n - 1) \cdot p_{atm} \cdot A + F_{cont} - mg \tag{4.18}$$

Eq. (4.18) can be normalized for h and t. Here, h is normalized to H^* (h/h_0) and t to T (ωt). The normalized form of Eq. (4.18) is

$$\frac{d^2 H^*}{dT^2} = \frac{1}{h_0 \omega^2}\left(\omega^2 Z_0 \sin T + \frac{(P_n - 1) \cdot p_{atm} \cdot A}{m} + \frac{F_{cont}}{m} - g\right) \tag{4.19}$$

Eq. (4.19) is a second-order nonlinear partial differential equation and its initial conditions (at t=0) are given as

$$\frac{dH^*}{dT} = 0 \tag{4.20}$$

$$P_n = 1 \tag{4.21}$$

$$F_{cont} = mg \tag{4.22}$$

The fourth-order Runge-Kutta method is used to solve the equation of motion (Eq. (4.19)). Eq. (4.19) is also coupled to the fluid dynamics of the squeeze film through the dimensionless mean pressure, P_n, calculated from the discretized Reynolds equation (Eqs. (4.3) and (4.10)).

4.2.2 Computational Scheme

The coupled dynamics (the Reynolds equation and the equation of motion) is solved simultaneously. Since the Reynolds equation is parabolic it must be solved at each individual step of the Runge-Kutta method. Fig. 4.4 illustrates the steps of an algorithm to solve the coupled dynamics. First, all constants, initial and boundary conditions are defined. Then the fourth-order Runge-Kutta method is implemented to solve the equation of motion. For each step of the Runge-Kutta method, the discretized Reynolds equation is solved to

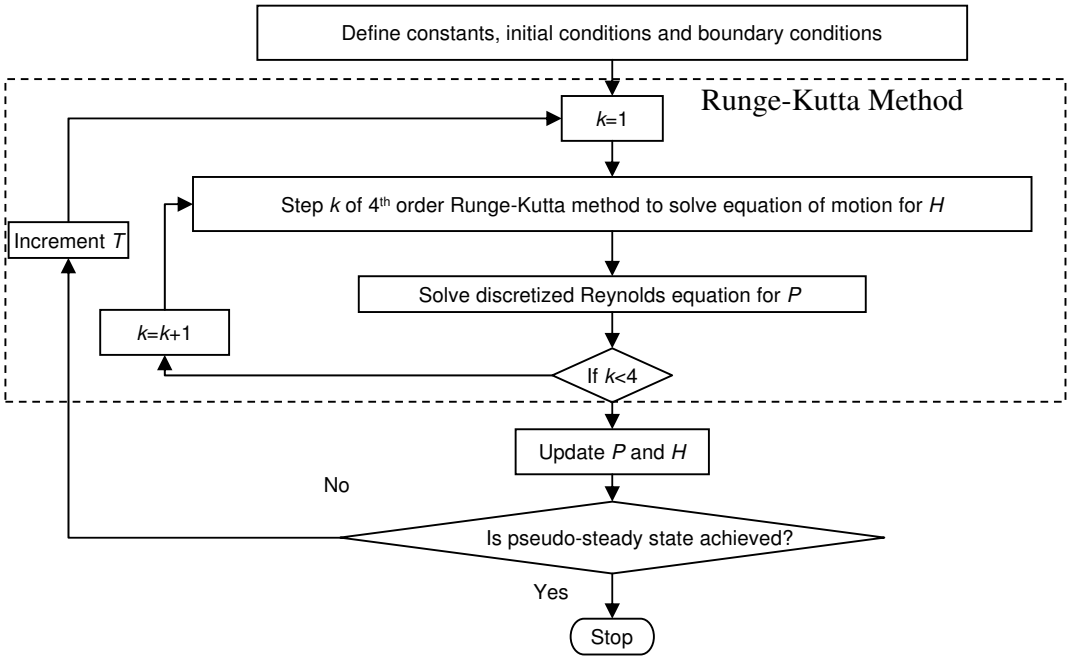

Figure 4.4: Algorithm for computational simulation

determine change in pressure due to change in the film height. This change in pressure is used in the next step of the Runge-Kutta method to account for change in the film height. Pressure and film thickness are updated at the last step. This process is continued until a pseudo-steady state is achieved. The simulation code is programmed in C (see Appendix B).

In order to confirm that the mesh density is adequate in space, only the discretized Reynolds equation is solved with an assumption that $\sigma = 1000$ and the squeeze film height is known as a function of time, i.e. H=1-0.5·sin(T). P as a function of T is plotted for 16 (Fig. 4.5) and 160 nodes (Fig. 4.6). From the plots (Figs. 4.5 and 4.6), it can be seen that the 16-node grid is as accurate as the 160-node grid. The deviation of pressure for grid size of 16 to that of 160 is only 0.75 %. Thus, the 16-node grid is used in numerical simulations in order to reduce computational effort.

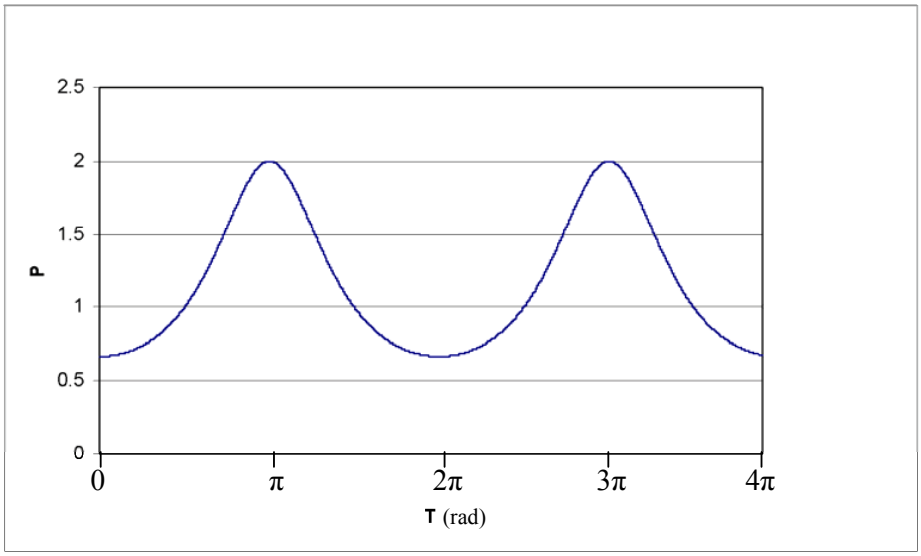

Figure 4.5: Dimensionless P as a function of normalized T at R=0.5, σ=1000 and H=1-0.5·sin(T) (16 nodes)

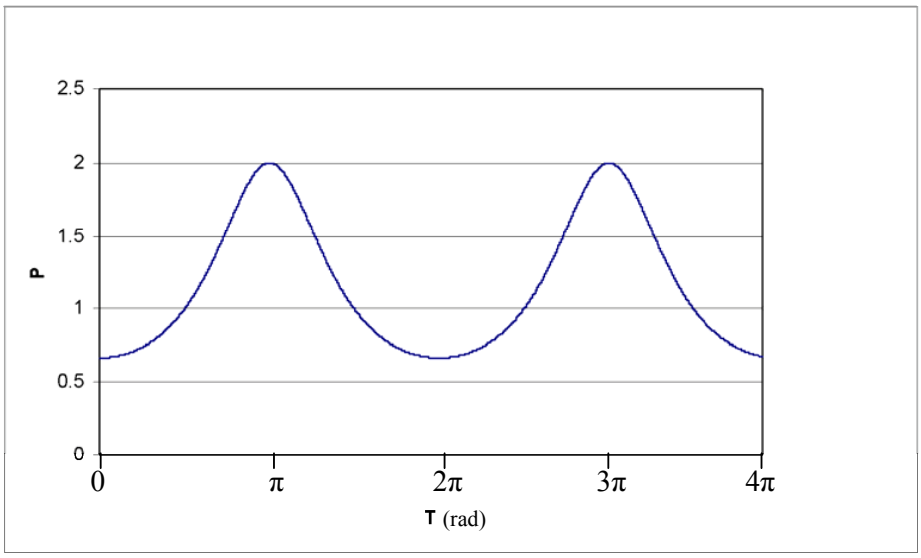

Figure 4.6: Dimensionless P as a function of normalized T at R=0.5, σ=1000 and H=1-0.5·sin(T) (160 nodes)

After defining the grid size, the value of the time-step Δt is refined by simultaneously solving the coupled dynamics. Fig. 4.7 shows that $\Delta t{=}\Delta T/\omega{=}10^{-7}$ s is small enough (deviation with step size, Δt of 10^{-8} s is 0.2214 %) and thus used to characterize squeeze film dynamics, but some error (deviation with step size, Δt of 10^{-8} s is 2.3868 %) occurs for $\Delta t{=}\Delta T/\omega{=}10^{-6}$ s.

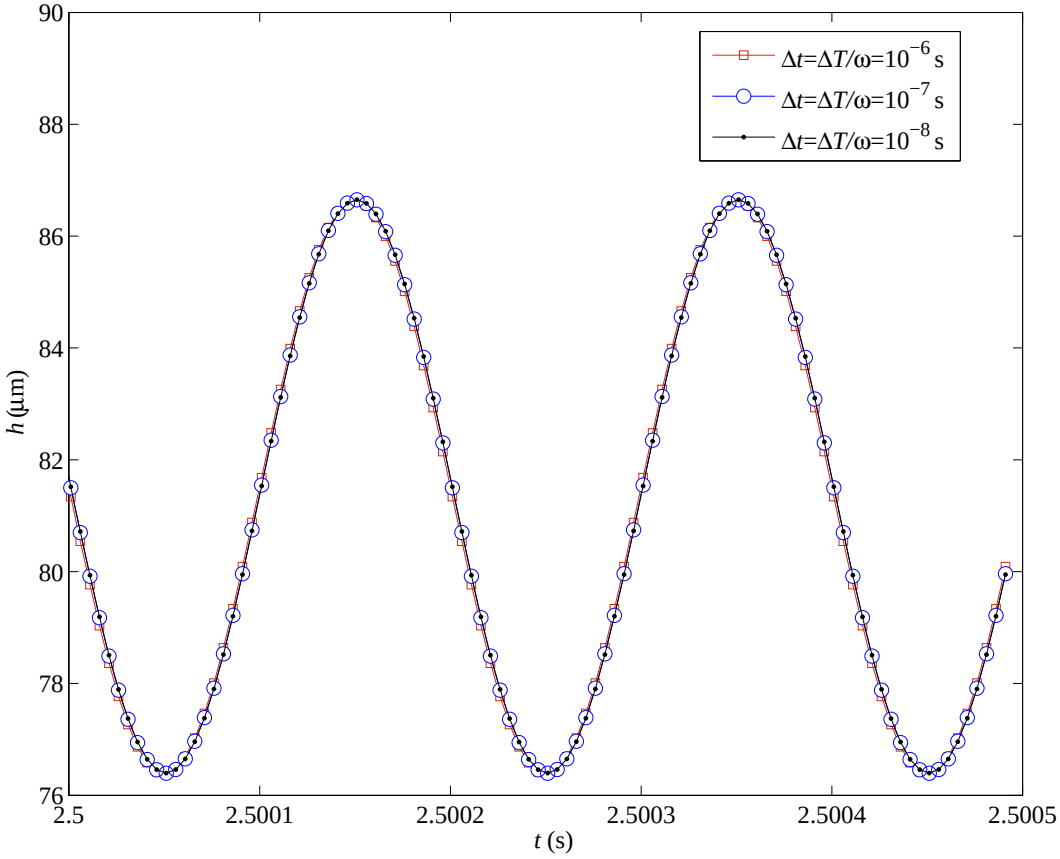

Figure 4.7: Variation in film height for different time steps

4.2.3 Results

The numerical simulation is performed from t=0 to the time when the squeeze film thickness achieves a pseudo-steady state (see Fig. 4.8). The simulation input parameters used are f =5000 Hz, Y=5 μm, R_0=0.0325 m and F_i=1.57 N. At t=0, film thickness is calculated solely from the contact force model and is used as an initial film thickness in the simulation. The base oscillation is initiated and the simulation is run to a pseudo-steady state.

Dynamic behavior of the squeeze film

From Fig. 4.8, it can be observed that between time 0 to 0.01 seconds the surfaces come in and out of contact and the contact force is dominant in this region. After 0.01 seconds, a full film is developed and the film height continues to increase until approximately 0.8 seconds. After approximately 0.8 seconds, the squeeze film achieves a pseudo-steady state where it oscillates at a mean squeeze film height (see Fig. 4.8 enlarged view). Simulation output parameters at pseudo-steady state are h_m=81.52 μm, ϵ=0.063 and σ=10.7.

Comparison with the pre-established models

Simulation results are used to verify the predictions of the squeeze film force model derived by Langlois [8]. The excursion ration, ϵ, and the squeeze number, σ, are substituted into Eq. (2.11) [8] and the squeeze film force, $F(T)$, is obtained. The squeeze film force, $F(T)$, from simulation result is $[(P-1)\cdot p_{atm}\cdot A]$. Fig. 4.9 shows that Langlois [8] and

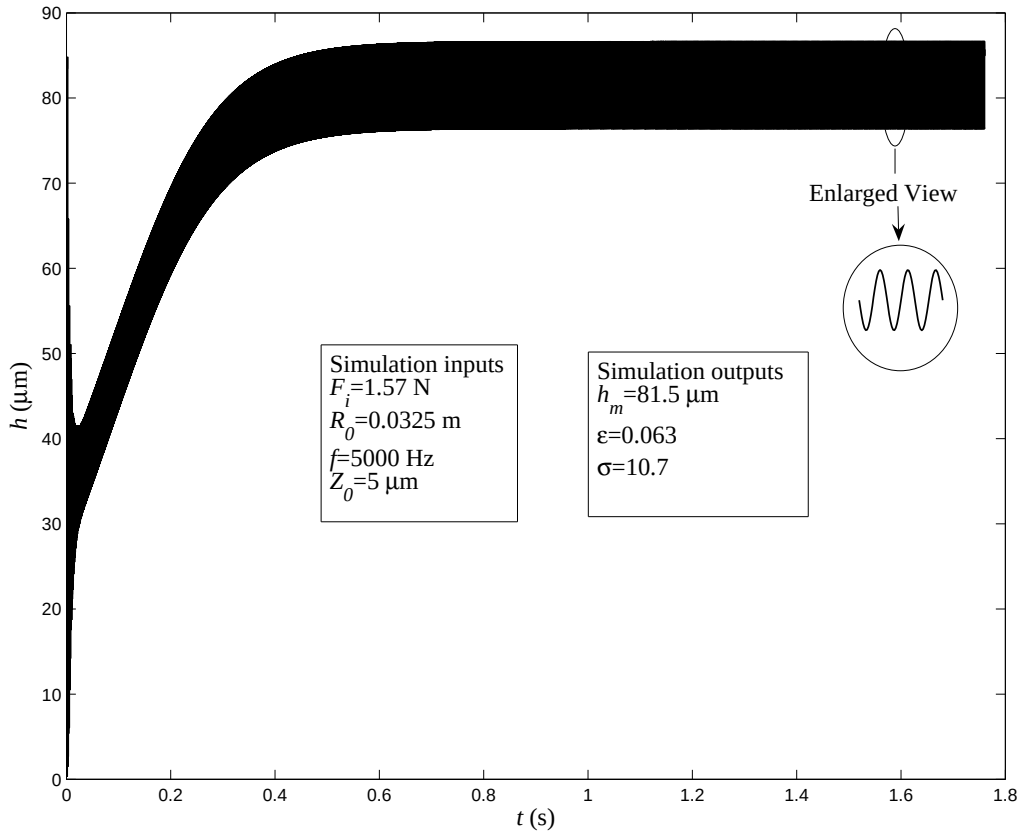

Figure 4.8: Dynamic behavior of the squeeze film height for given input conditions as a function of time

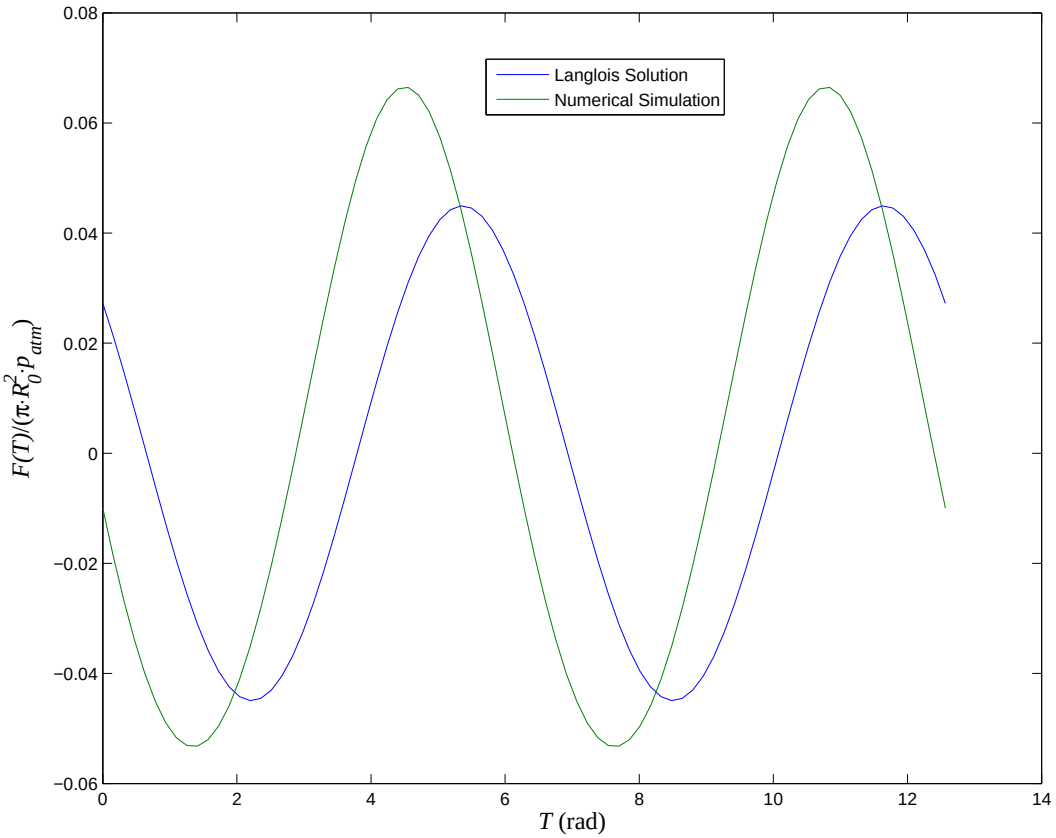

Figure 4.9: Comparison of the dimensionless squeeze film force, $F(T)/(\pi \cdot {R_0}^2 \cdot p_{atm})$, as a function of normalized time, T, from the numerical simulation and from Langlois squeeze film force model [8]

present model compare moderately well and so [8] approximately predicts the periodic squeeze film force. Since $F(T)$ given by [8] is a function of sine and cosine (Eq. (2.11)), the net squeeze film force over one period is zero. This does not hold true because the numerical analysis and Salbu [9] predict a net load carrying force is formed. Thus, $F(T)$ by [8] is a good estimation but is not entirely accurate. As per the present model, the net squeeze film force over one period equals to the weight of the levitating disk.

The excursion ratio, ϵ, and the squeeze number, σ, calculated from the current simulation results (See Fig. 4.8) can also be used to verify and correlate with the predictions of Salbu's Eq. Substituting values R_0=0.0325, f=5000 Hz and h_m=81.5 μm (See Fig. 4.8) into Eq. (2.10) gives squeeze number, σ=10.7. As σ is greater than the limiting minimum value of 10 defined by Salbu [9], Salbu's Eq. can be used to calculate the load carrying capacity. A comparison of the applied load, F_i and predicted load, F_n by Salbu's Eq. is shown in Table 4.1.

Table 4.1: Comparison of load carrying capacity between F_i in numerical simulation and F_n by Salbu's Eq.

F_i	1.57 N
F_n by Salbu's Eq. for ϵ=0.063	1.67 N
Percentage error between F_i and F_n	6.4

As the percentage error between F_i and F_n by Salbu's Eq. is only 6.4; it appears that the coupled model is in agreement with the pre-established model [9] and can be used to study the dynamic behavior of squeeze film bearings. More extensive comparisons of the simulation results to Salbu's predictions are presented in the next section.

Development of Semi-analytical Equation

Simulations are performed by changing the simulation parameters such as f, R_0, Z_0 and F_i. Thus a wide range of values for σ ($0.4<\sigma<14.6$) are obtained. Also the percentage error between F_i and F_n by Salbu's Eq. is calculated for these simulations. For $\sigma>10$, it is observed that the percentage error between F_i and F_n by Salbu's Eq. is fairly low (less than 7). However, for $\sigma<10$, the percentage error increases and over-predicts the load carrying capacity (Fig. 4.10). Thus, Salbu's Eq. can be used as a basis to calculate load carrying capacity if σ is greater than 10, but if it is less than 10, the percentage error increases significantly and a modified form of Salbu's Eq. is needed. In order to obtain a semi-analytical equation to extend the range of Salbu's Eq., it is modified by the curve fitting technique using the percentage error between F_i and F_n as predicted by Salbu's Eq. Here, the level of certainty of the fit is 95 % and value of R-square is 0.9985. An exponential equation $f(\sigma)$ is fit to the percentage error of the data as a function of σ (see Fig. 4.10) and is given by

$$f(\sigma) = 460 \cdot exp(-4.5 \cdot \sigma) + 19 \cdot exp(-0.15 \cdot \sigma) \tag{4.23}$$

$$W_n = \frac{F_n}{\pi p_{atm} {R_0}^2} = \left(\frac{1}{1+f(\sigma)}\right)\left\{\left[\frac{1+\frac{3}{2}\epsilon^2}{1-\epsilon^2}\right]^{1/2} - 1\right\} \tag{4.24}$$

A comparison between F_i and F_n using Eq. (4.24) for a large number of points within $0.4<\sigma<10$ is performed. It is observed that the average percentage error between F_i and

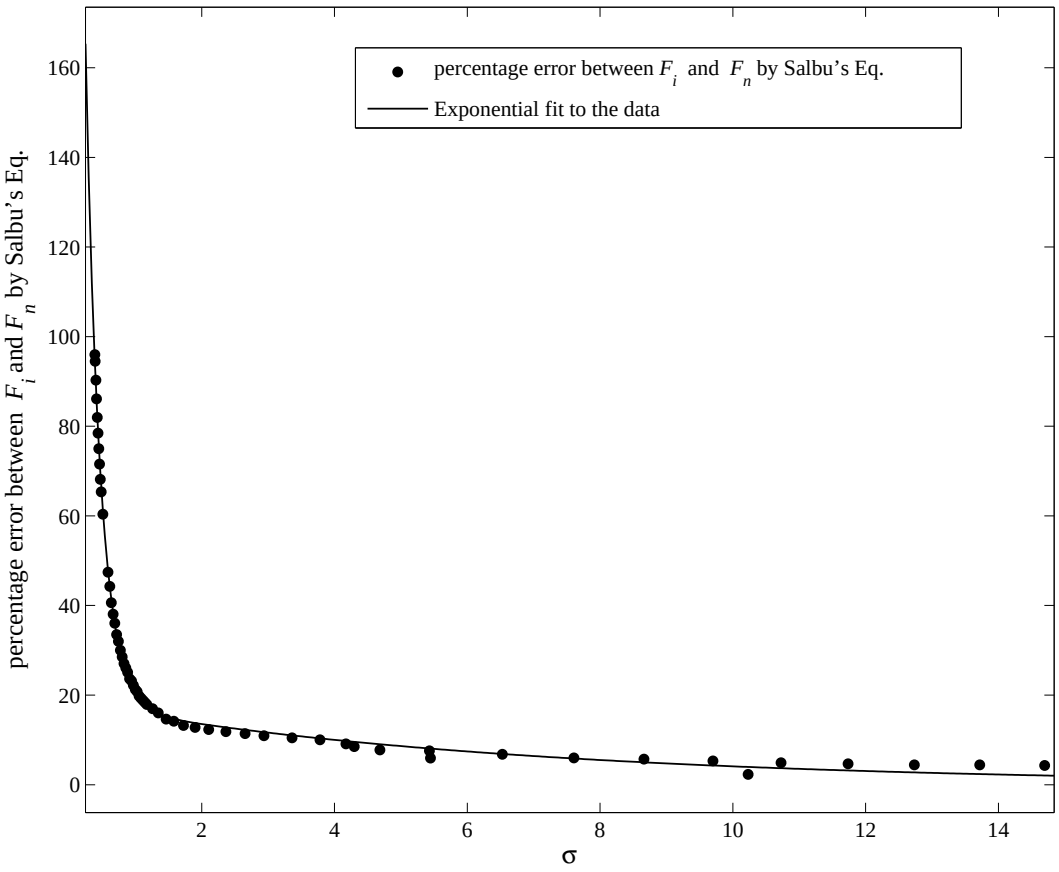

Figure 4.10: Change in percentage error between F_i from the numerical simulation and F_n as predicted by Salbu's Eq. as a function of the squeeze number, σ

F_n from Eq. (4.24) for $0.4<\sigma<10$ is only 1.04. Thus Eq. (4.24) confirms its usefulness for lower σ values in this range.

Parametric Study

A parametric study using the analytical simulation is performed to study the behavior of the mean squeeze film height as a function of F_i (Fig. 4.11). As shown, h_m decreases with increases in F_i, for a given set of simulation parameters. It can also be observed from Fig. 4.11, that if the frequency is doubled and other parameters kept constant, the mean squeeze film height, h_m, changes but relatively less than when load is varied. The variation of h_m with F_i is similar in nature for both the frequencies. Numerical simulations are performed to study the behavior of the mean squeeze film height as a function of the amplitude of vibration, Z_0. An experimental investigation is also performed to study the behavior of the mean squeeze film height as a function of Z_0. Both numerical and experimental results are compared, and so the results are presented in the next chapter on the experimental work.

The behavior of the mean squeeze film height, h_m, as a function of frequency, ω, is also studied by keeping all other simulation parameters (m=6.97 gm, R_0=9 mm and Z_0= 5 μm) constant. It can be observed from Fig. 4.12, that if the frequency, ω increases, the mean film height also increases. For lower frequencies, the slope of the graph is higher which indicates more increase in the mean squeeze film height with increase in frequency. For higher frequencies, the slope of the graph is lower which indicates less increase in the mean squeeze film height with increase in frequency.

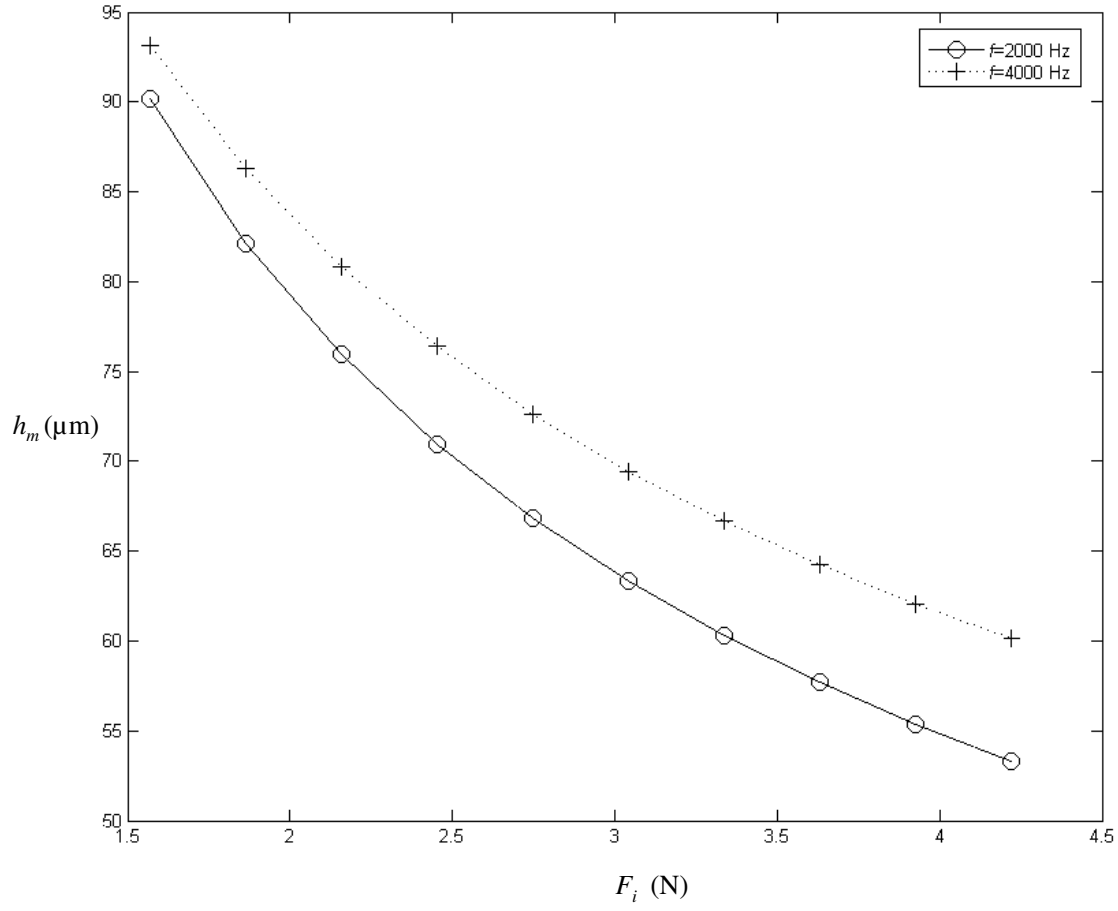

Figure 4.11: The results of numerical parametric study for h_m as a function of F_i at a constant frequency

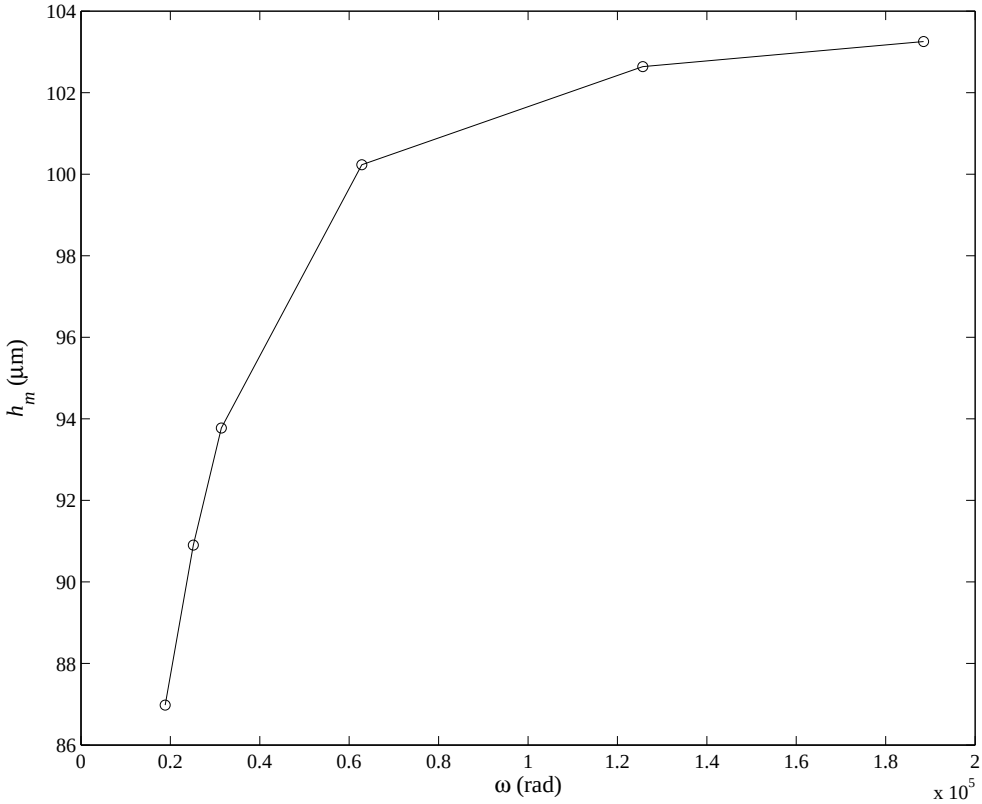

Figure 4.12: The results of numerical parametric study for h_m as a function of ω

4.3 Ultra-Thin Squeeze Film Bearings

From the background (Section 2.7), if the squeeze film bearing operates in the slip, transition or molecular flow regime then the bearing is considered as an ultra-thin squeeze film bearing. This section covers the formulation of the coupled dynamics and computational scheme as it differs from the thin squeeze film bearings.

4.3.1 Formulation of Coupled Dynamics

The dynamics of the ultra-thin squeeze film bearings is generally the same as the thin squeeze film bearings except in the ultra-thin squeeze film bearings, a modified form of the Reynolds equation is used.

$$\frac{1}{R}\frac{\partial}{\partial R}\left(RH^{*3}P\frac{\partial P}{\partial R}\right) = {\sigma^*}_{eff}\frac{\partial\left(PH^*\right)}{\partial T} \tag{4.25}$$

where ${\sigma^*}_{eff}$ is as given

$${\sigma^*}_{eff} = 12\mu_{eff}{R_0}^2\omega/p_{atm}{h_0}^2 \tag{4.26}$$

The effective viscosity, μ_{eff}, is given by Eq.(2.28) [38] which accounts for the gas rarefaction effects. The discretization scheme for the left hand side of Eq. (4.25) and the boundary conditions are the same as that used for the thin squeeze film bearings (See Eqs (4.3)-(4.9)).

The right hand side of Eq. (4.25) is discretized as

$$\sigma_{eff}{}^{*}\frac{\partial\left(PH^{*}\right)}{\partial T} \approx \sigma_{eff}{}^{*}\frac{P_{i,j+1}H^{*}{}_{j+1} - P_{i,j}H^{*}{}_{j}}{\Delta T} \tag{4.27}$$

The equation of motion, Eq.(4.19), is the same for both thin and ultra-thin squeeze film bearings. The initial conditions are given by Eqs. (4.20)-(4.22).

4.3.2 Solution Methodology

The algorithm (Fig. 4.13) to solve the coupled dynamics (the modified Reynolds equation Eq. (4.25) and the equation of motion Eq. (4.19)) for the ultra-thin squeeze film bearing is same as the thin squeeze film bearings (Eqs. (4.1) and (4.19)) except for one change. Here, the modified squeeze number, $\sigma^{*}{}_{eff}$ is calculated each time before solving the discretized Reynolds equation.

4.3.3 Results

A computer program (see Appendix E) as per the algorithm detailed in Fig. 4.13 is written to solve the discretized Reynolds equation (Eqs. 4.22 and 4.24). Here, the squeeze film thickness is assumed as a known function of time and only the modified Reynolds equation (Eqs. 4.22 and 4.24) is solved. Simulation and experimental results are compared and the results are presented in the next chapter (see Section 5.2.3).

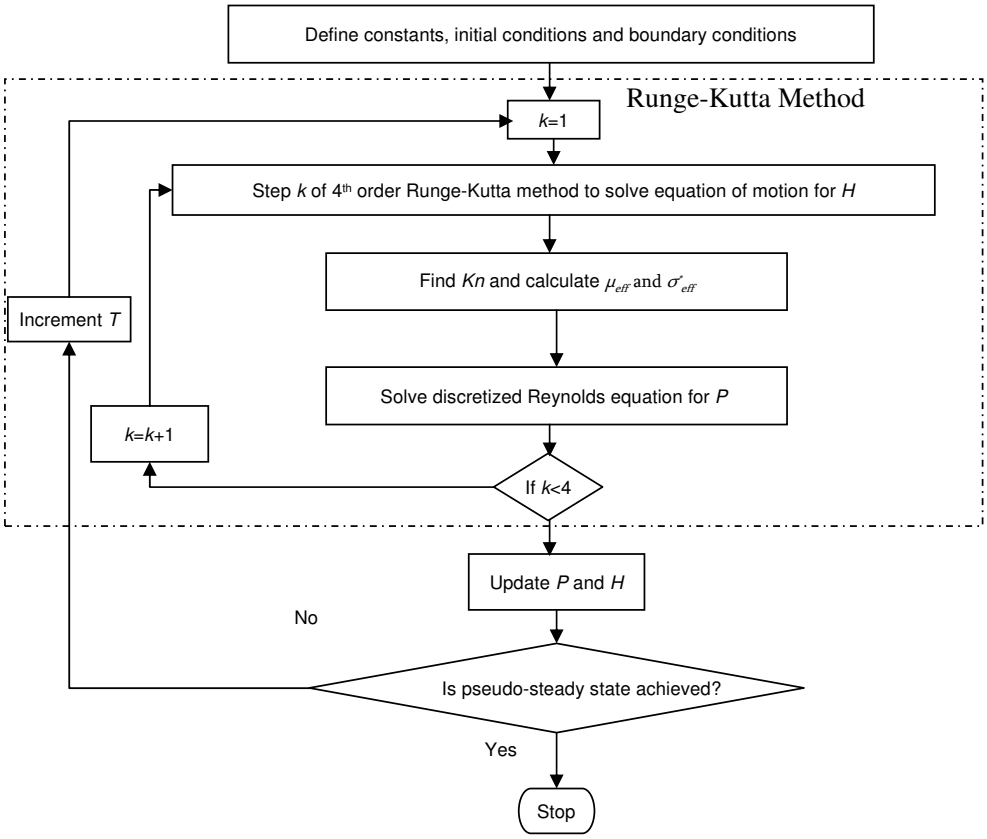

Figure 4.13: Algorithm for computational simulation of the ultra-thin squeeze film bearing

Chapter 5

Experimental Investigation

5.1 Thin Squeeze Film Bearings

This section covers in detail the effort taken towards reaching the goal of generation, control and measurement of the squeeze film between two bearing surfaces. The different techniques for the measurement of the squeeze film height are described here followed by a discussion of the results.

5.1.1 Experimental Setup

A test rig (See Fig. 5.1) has been built in order to generate a squeeze film and measure the squeeze film thickness. The experimental setup is used to perform a parametric investigation with the variation of frequency, amplitude of vibration and mass of the levitating disk. Each subsystem of the experimental setup is described in detail.

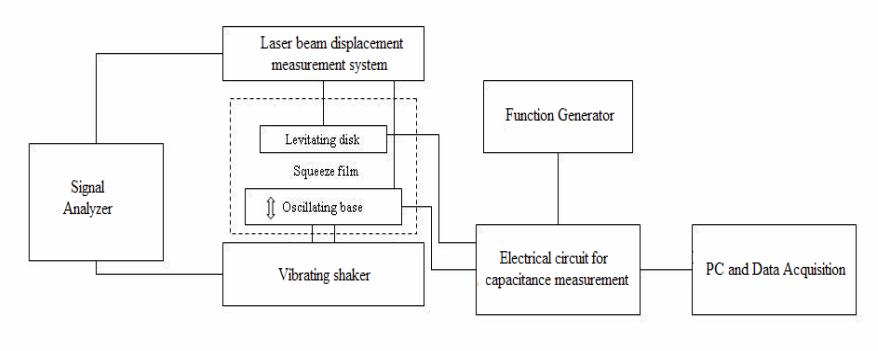

Figure 5.1: Schematic explaining the experimental setup

Test Stand

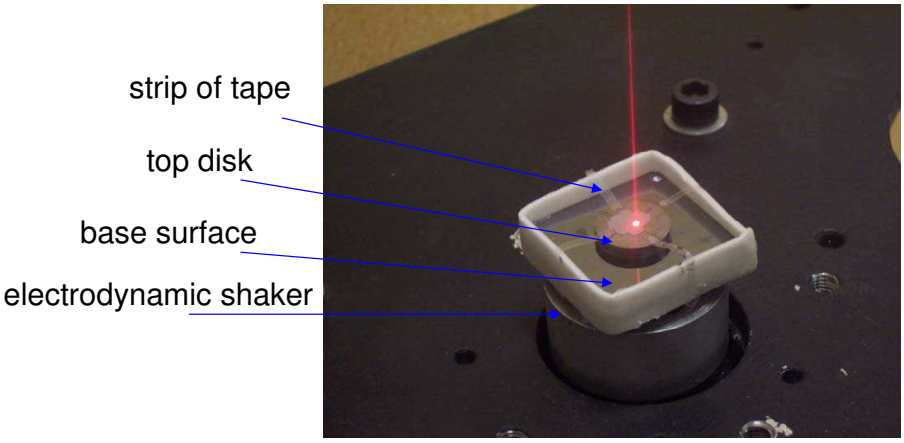

Figure 5.2: Test stand used for experimental investigation

A rectangular bracket holding the lower bearing surface is used as an oscillating base (See Fig. 5.2). On the top of the lower bearing surface a disk is placed. The top disk is tethered to the rectangular bracket using four small strips of tape. This attachment is done in such a way that the top disk can only float with one degree of freedom i.e permitting the motion only in vertical direction. This setup may result in additional load being placed on the bearing. Different disk sizes used for levitation can be seen in the Fig. 5.3 and their specifications are tabulated in Table 5.1.

Table 5.1: Bearing configurations used for the experimental purpose

Configuration	**Radius (mm)**	**Mass (g)**
1	32.5	160
2	7.5	2.62
3	9	6.97

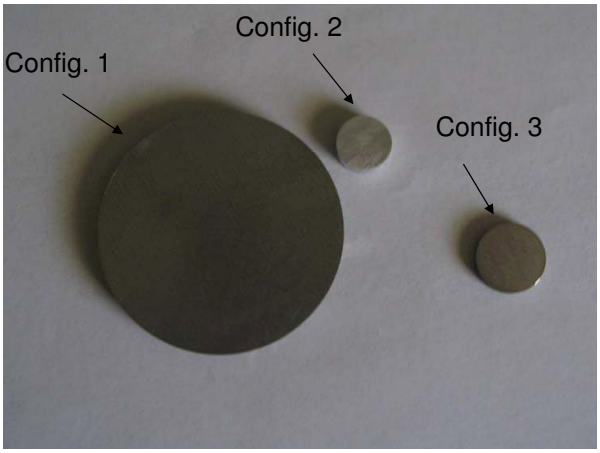

Figure 5.3: Disks used for levitation

Electrodynamic shaker

The test stand is fastened to an electrodynamic shaker (LDS Model V408) (See Fig. 5.4 and 5.6). The electrodynamic shaker provides sinusoidal oscillations to the lower bearing surface.

Gain Control and Dynamic Signal Analyzer

A gain control (LDS PA 500L amplifier) and a dynamic signal analyzer (HP 3566 5A) are used together for vibration control (Fig. 5.4 and 5.6). The source from the dynamic signal analyzer is set as a sine wave. The frequency of the source is set to a fixed value and the level of the source is changed to vary the amplitude of the vibration. The output from this source is given to the gain control mechanism which sends the signal to the electrodynamic shaker.

A dynamic signal analyzer is also used to read the amplitude of vibration of the oscillating base as given by a laser beam displacement measurement system (LBDMS). It records the analog voltage from the LBDMS. The amplitude of this analog voltage is then converted into the amplitude of oscillation of the bearing surfaces in microns(μm) by multiplying the scale set on the LBDMS. The LBDMS is discussed in greater detail later.

Capacitance sensor

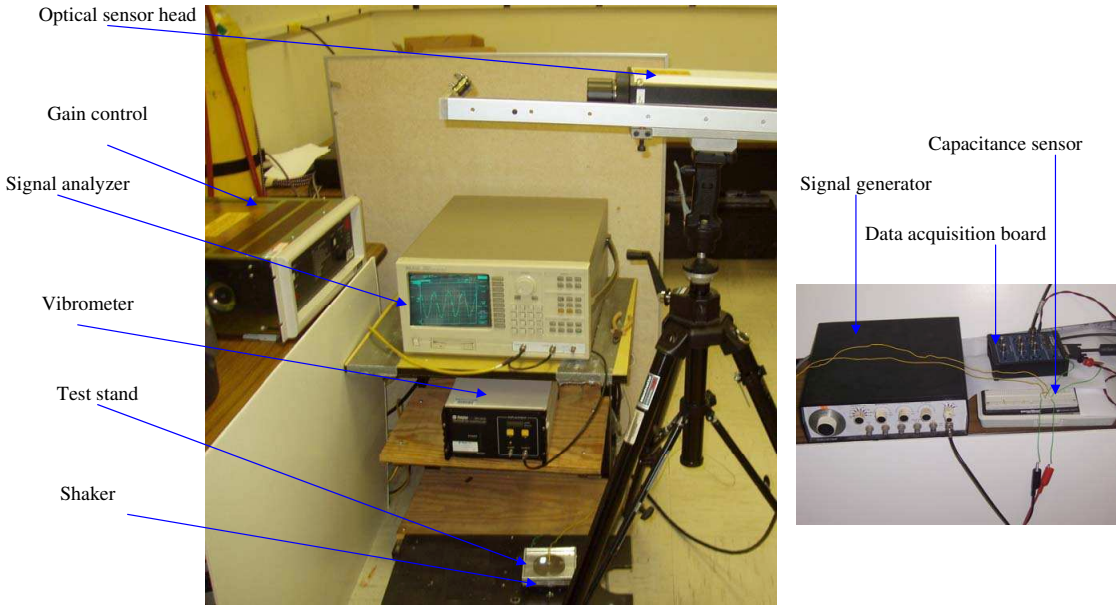

Figure 5.4: Photograph illustrates the experimental setup with the capacitance sensor

If there is a gas squeeze film between two parallel plates then the plates form a parallel plate capacitor with air as the dielectric. The capacitance between two parallel plates is

theoretically given as

$$C = \frac{A\epsilon_0 k}{d} \tag{5.1}$$

Thus, a capacitance sensor (Fig. 5.4) is built in order to measure the capacitance between the base and the levitating disk and then calibrated (Appendix D) to provide the squeeze film height in microns. First, electrical connections are made to both the bearing surfaces. The electrical circuit in Fig. 5.5 [46] is built to measure the capacitance due to an air-gap between these surfaces. V_{in} is the input voltage to the electrical circuit which is provided

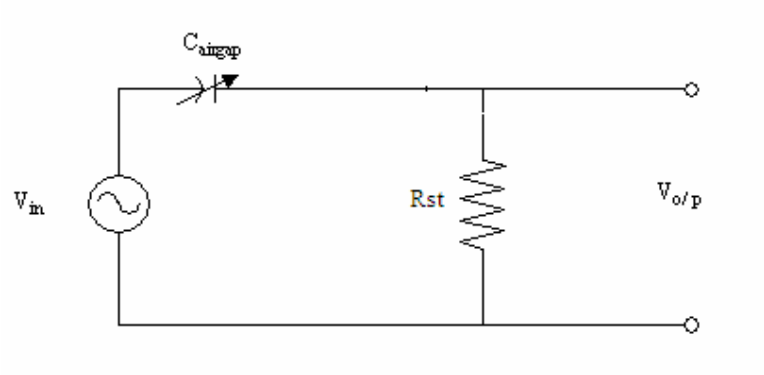

Figure 5.5: Electrical circuit for capacitance measurement

by the signal generator. The frequency of AC input voltage is set to 2000 Hz and RMS V_{in} is set to 7.07 V. *Rst* is a standard resistor with a value of 33 kΩ. C_{airgap} is the parallel plate capacitor formed by the two bearing surfaces across which $V_{o/p}$, output voltage is measured by a data acquisition system, NI BNC 2140. The voltage ratio (RMS output voltage/RMS input voltage) is needed to calculate the capacitance (see Appendix D). This capacitance

between the parallel plates is then calibrated using thin film shims to provide squeeze film height. Thus, using this experimental set-up, the squeeze film lift and height generated between the plates can be measured.

Laser Beam Displacement Measurement System

Figure 5.6: Photograph illustrates the experimental setup with the laser displacement measurement system

The LBDMS used comprises of an optical sensor head (Polytec OFV 2610) and a laser vibrometer (Polytec OFV 2610)(See Fig. 5.6). The laser beam is incident on the top levitating disk by an optical sensor head. An analog voltage signal proportional to the displacement of the top disk is then available at the output of the laser vibrometer. The scale on the laser vibrometer is set to the finest value of 20 μm/V and the resolution at this scale is 0.08 μm. This analog voltage is given as an input to the data acquisition system

(NI BNC 2140). National Instrument's LabView is used to record the DC estimate of the input analog signal at a given scan rate in a text file. This text file is later imported and plotted by MATLAB (Fig. 5.7) for further analysis. The change in DC voltage from the initial to final state multiplied by 20 μm/V gives the squeeze film height in microns. For instance, the average measured film thickness of the experimental results shown in Fig 5.7 is 17.15 μm.

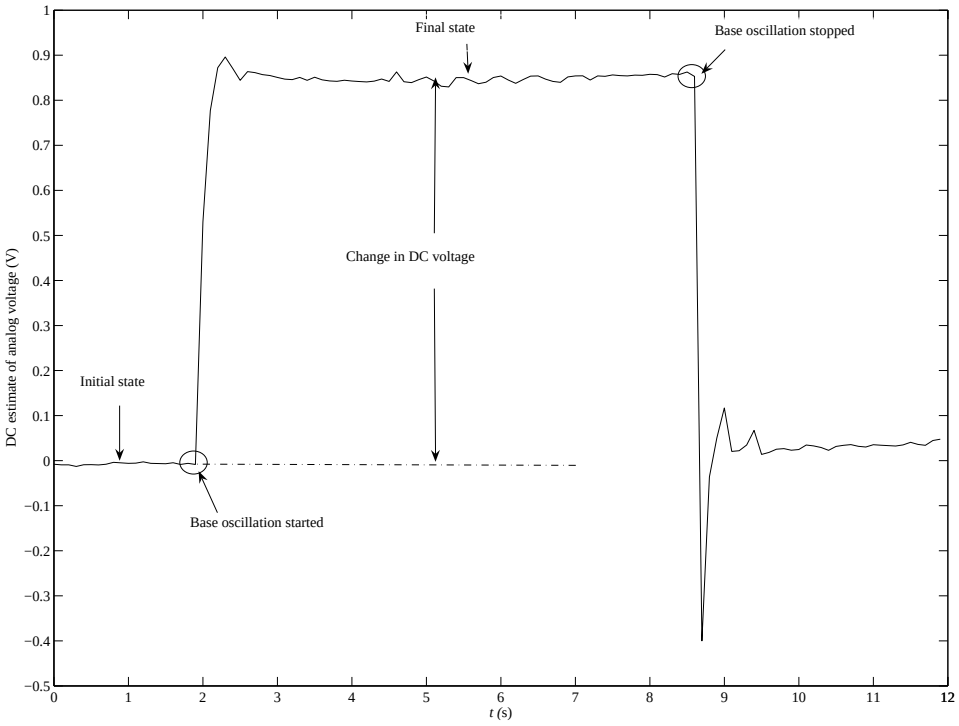

Figure 5.7: Plot of DC voltage from the laser beam displacement measurement system

5.1.2 Experimental Results

Configuration 1

A comparison between the experimental and the numerical results is first made using the capacitance measurement system on configuration 1 (See Appendix C, Section C1). Results are plotted for the mean squeeze film height as a function of the amplitude of vibration for several frequencies (See Fig. 5.8). These numerical results show that, for an increase in the amplitude of vibration, Z_0, there is a corresponding increase in the mean squeeze film height, h_m, if all other parameters remain unchanged. The experimental results for configuration 1 agree qualitatively but the offset between the experimental and the numerical results is large. h_m for configuration 1 is measured using the capacitance sensor. It is observed that small metal particles or dust between two surfaces can significantly affect the capacitance measurements, which requires that the surfaces must be frequently cleaned between tests. It should also be noted that the surfaces of this configuration have significant imperfections (i.e. roughness and waviness). Even after cleaning the surfaces, during the start-up of the test, initial contact may create small wear particles and the absolute cleanliness of surfaces cannot be guaranteed. This makes the capacitance measurements difficult and also not repeatable, LBDMS is used to record the film thicknesses for configurations 2 and 3 which are also smoother.

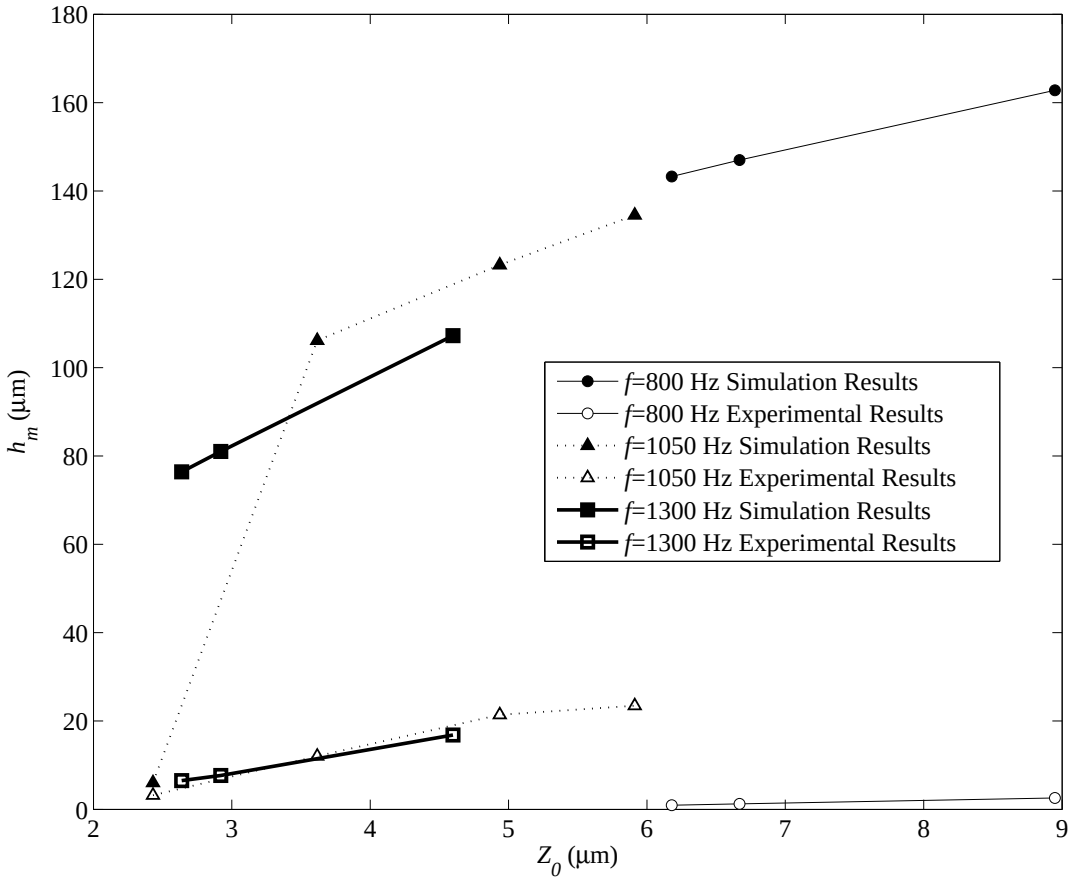

Figure 5.8: Experimental and simulation results for the squeeze film height against the amplitude of vibration for bearing configuration 1 (Capacitance measurement system)

Configuration 2

The plot in Fig. 5.9 shows the squeeze film thickness plotted as a function of the amplitude of vibration for the base. The measurements are made using LBDMS. Each test is run ten times in order to assure the repeatability of the setup. The average standard deviation of the test data (See Appendix C, Section C2) is found out to be 0.31 μm, and thus it can be said that experiments show good repeatability. It can be seen from Fig. 5.9 that if the frequency is small then it takes a higher amplitude to generate the squeeze film height. Conversely, if the frequency is increased then the amplitude of vibration is lower. These qualitative trends are also agreed by the theoretical results as discussed earlier. For configuration 2, both simulation and experimental results match qualitatively but the offset between them is very high. Also, there is a convergence problem for configuration 1 (Fig. 5.9) for lower frequencies and amplitudes. For such cases, the solution did not converge to a pseudo-steady state even after running simulations for a longer duration.

Configuration 3

Measurements are also carried out for configuration 3 (See Appendix C, Section C3) using LBDMS and the average standard deviation for configuration 3 is found to be 0.18 μm which suggests that experiments are repeatable. Observations for configuration 2 (Fig. 5.9) and configuration 3 (Fig. 5.10) are similar in nature. The average deviation between numerical and experimental data is calculated to be 44 μm ($\approx$ 73 %) from the results of configurations 2 and 3. For a similar type of comparison with the results of [10], the average

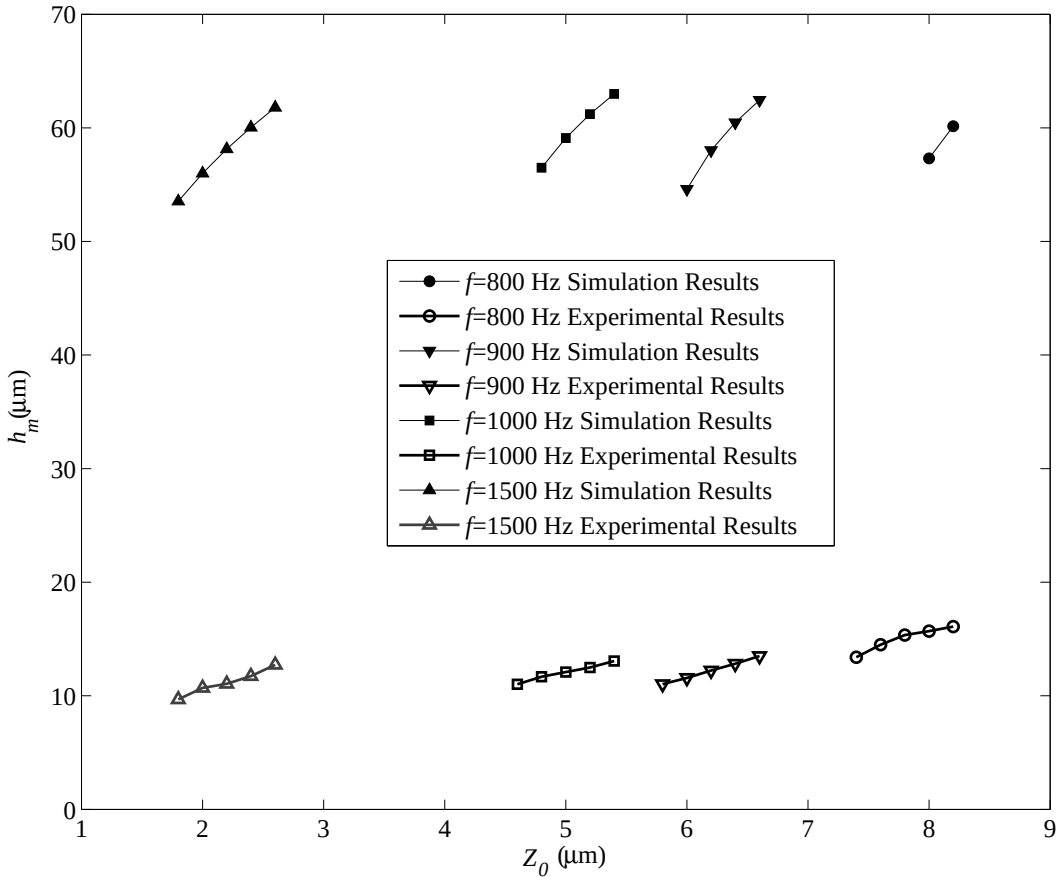

Figure 5.9: Experimental and simulation results for the squeeze film height against the amplitude of vibration for bearing configuration 2 (Laser displacement measurement system)

deviation is 38 μm ($\approx$ 51 %). From this comparison, it should be noted that both Minikes and Bucher [10] and a current numerical simulations overestimate the film thickness by similar magnitudes. This is because the assumptions made in the numerical model cannot be perfectly implemented while conducting experiments. The numerical model assumes that the disks are flat and rigid, and that the system has a single degree of freedom (motion only in the vertical direction). However, during the experimental tests, it is observed that there is a component of motion acting in the horizontal plane. The surfaces are not perfectly flat due to surface roughness and waviness and consequently are not perfectly leveled. Thus, the assumption of a planar squeeze film cannot be experimentally achieved. It is possible to include the effects due to tilting of the squeeze film in the theoretical work to achieve a better comparison but it will lead to a much more complex theoretical model. The other possible reasons for differences between the analytical and experimental results can be attributed to dust or small wear particles present in between the plates, misalignment between the surfaces, and the sensitive nature of the laser setup to external vibrations. However, the experimental results do confirm that the squeeze film effect can be used in real applications to generate gas squeeze film bearings.

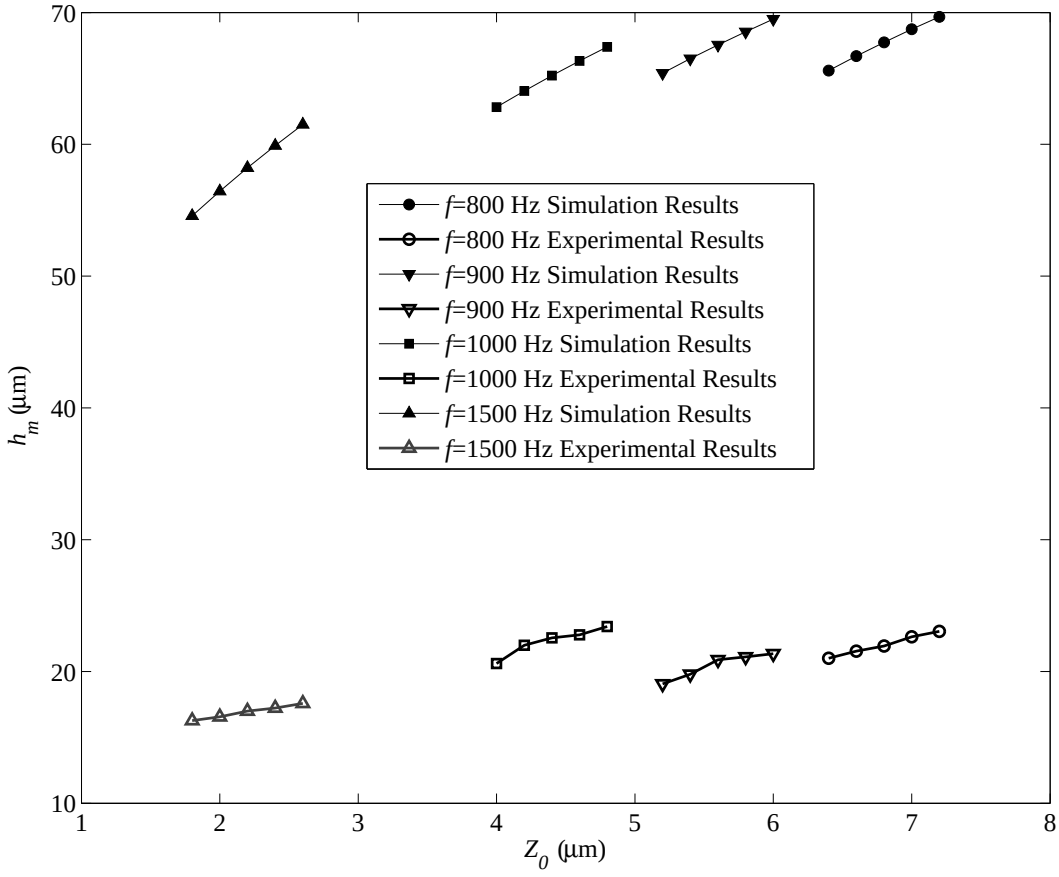

Figure 5.10: Experimental and simulation results for the squeeze film height against the amplitude of vibration for bearing configuration 3 (Laser displacement measurement system)

5.2 Ultra-thin Squeeze Film Bearings

This section covers in detail the design and fabrication of micro-scale squeeze bearing surfaces which is later used for the testing of ultra-thin squeeze film bearings. LASICAD software is used for the design of micro-scale bearing surfaces and the fabrication is carried out in the Alabama Microelectronics Science and Technology Center.

5.2.1 Design of Micro-Scale Bearing Surfaces

See Fig. 5.11 for an enlarged view of examples of the LASICAD drawing for each surface. Here, the relative scale between different geometries is preserved. Three circular geometries (Diameter 10, 50, 100 μm) and one square geometry (50 μm X 50 μm) are drawn using LASICAD. Each sample micro bearing surface represents a grid of a particular geometry on a 3 cm X 3 cm square. For example, a sample bearing surface (Fig. 5.11 top left) is a grid of 50 μm diameter circular areas where the centers of two consecutive areas are separated 100 μm apart. Other samples are also seen in Fig. 5.11 where top right represents a grid of 50 μm X 50 μm squares, bottom left represents a grid of 10 μm diameter circles and bottom right represents a grid of 100 μm diameter circles. As per the LASICAD drawing, a TLD (Transportable LASI Drawing) file is utilized to externally fabricate the photomask. The photomask is a square glass plate having the drawing encapsulated on a chromium layer.

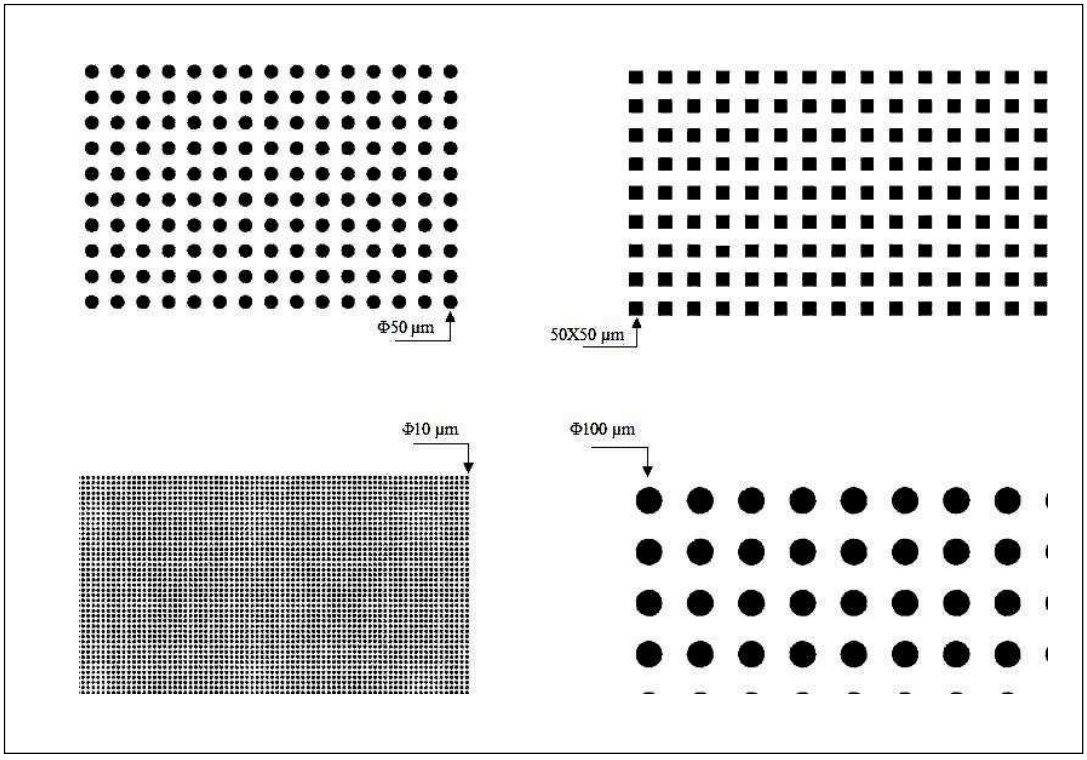

Figure 5.11: LASICAD drawing of micro bearing surfaces (not to scale and only portions of the textured sections are shown in this enlarged view)

5.2.2 Fabrication of Micro-Scale Bearing Surfaces

The process flow of fabrication of micro bearing surfaces is diagrammed in Fig. 5.12. The steps involved in this fabrication are described as below.

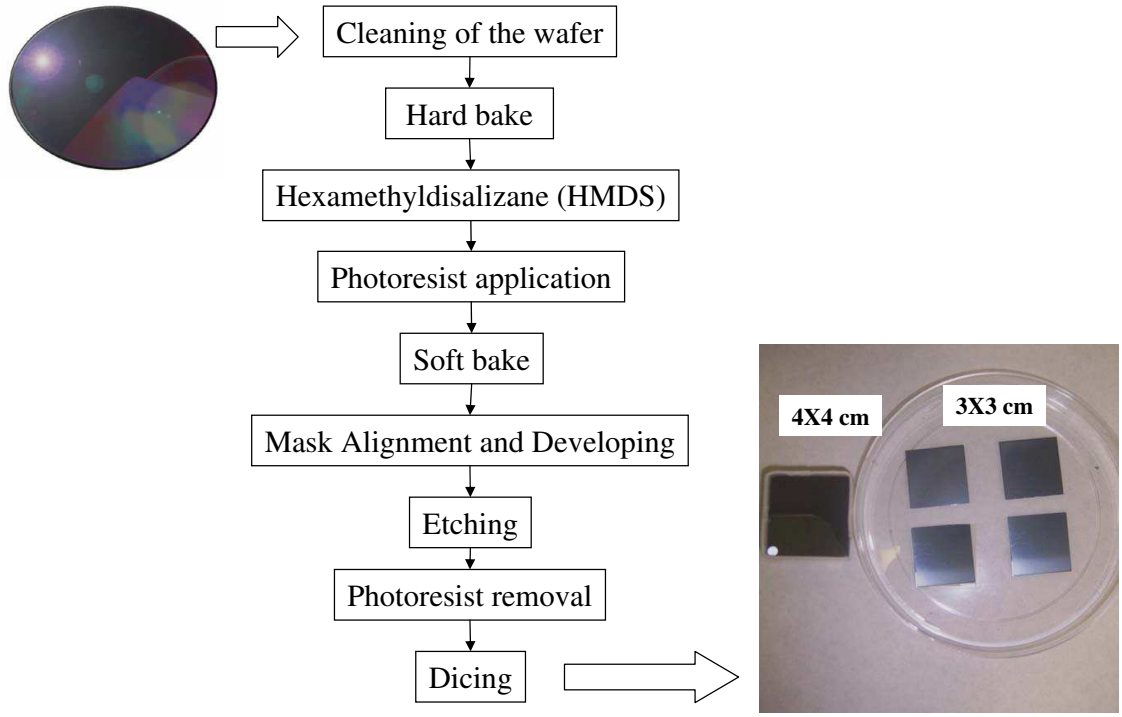

Figure 5.12: Fabrication procedure for micro-scale bearing surfaces

Cleaning of the wafer

A new silicon wafer of p-type and surface orientation $< 100 >$ is cleaned as per the B, C, and D silicon wafer cleaning procedure (See Table 5.2 [42]).

Table 5.2: Silicon Wafer Cleaning Procedure [42]

B	Removal of Residual Organic/Ionic Contamination	
	1	Hold a wafer in a (5:1:1) solution of $H_2O - NH_4OH - H_2O_2$ for 10 min at a temperature of 75-80 ^{0}C
	2	Quench the solution under running deionized (DI) water for 1 min
	3	Clean a wafer in DI water for 5 min
C	Hydrous Oxide Removal	
	1	Immerse a wafer in a (1:50) solution of $HF - H_2O$ for 15 sec
	2	Clean a wafer under running DI water for 30 sec
D	Heavy Metal Clean	
	1	Hold a wafer in a (6:1:1) solution of $H_20 - HCl - H_2O_2$ for 10 min at a temperature of 75-80 ^{0}C
	2	Quench the solution under running deionized (DI) water for 1 min
	3	Clean a wafer in running DI water for 20 min

Hard bake

Hard baking of the wafer is done by an Imperial IV microprocessor oven. The wafer is kept inside the oven for 20 minutes at 120 ^{0}C. The hard bake process removes any moisture content from the wafer.

Hexamethyl disalizane (HMDS)

After the hard bake, the wafer is kept in a HMDS chamber for 20 minutes. Here, the wafer surface is primed with HMDS to promote better adhesion to the photoresist.

Photoresist application

Photoresist is a light-sensitive material to which patterns are first transferred from the photomask. A liquid photoresist (AZ 5214) is applied in a liquid form onto the wafer

surface. Then the wafer held on a vacuum chuck undergoes rotation at a speed of 3000 rpm for 40 sec. This process provides a layer of photoresist of even thickness.

Soft baking

The photoresist-coated wafer is then transferred to a hot plate for soft baking or pre-baking. Soft baking is performed on a hot plate at 105 ^{0}C for 1 minute. It improves the adhesion of the photoresist to the wafer and also drives off solvent from the photoresist before the wafer is introduced into the exposure system.

Mask Alignment and Exposure

In this step, the photo mask is aligned with the surface of the wafer. The wafer is held on a vacuum chuck, and moved into position below the photo mask. The spacing between the photo mask and wafer surface is in the range of 25 to 125 μm. Following alignment, the photoresist is exposed for 10 seconds with high-intensity ultraviolet light. After this step, the wafer is developed in the AZ 514 developer.

Etching

Etching is performed to remove material between the circular and square areas so that micro-scale bearing areas are formed on the wafer (in the form of posts). These micro-scale bearing areas can be observed as posts protruding out from the base silicon. Deep reactive ion etching is used to etch out the wafer. The machine used for this process is Surface Technology System's (STS) advanced silicon etcher. An etch depth of approximately 80

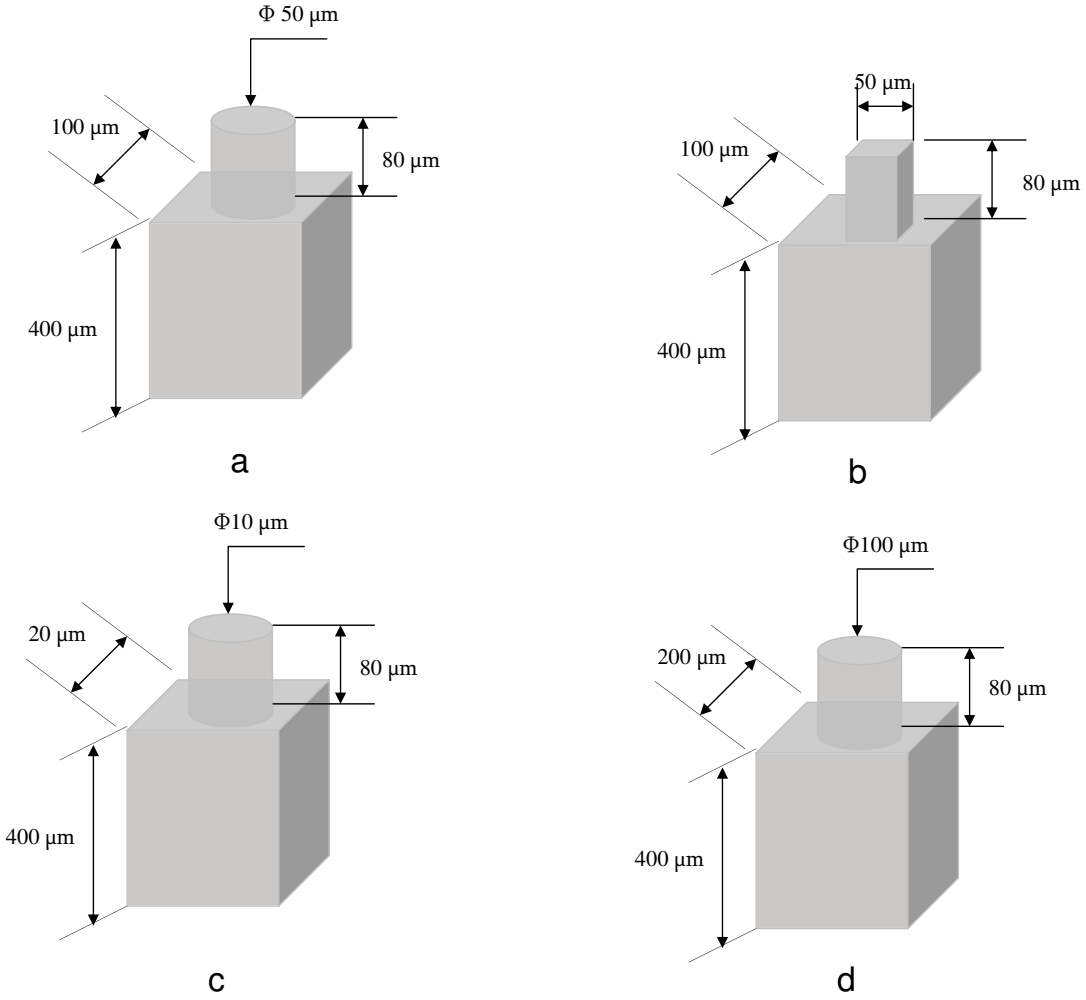

Figure 5.13: Schematics of single unit cell (not to scale)

μm is achieved from 120 cycles of Morgan SOS 1 process. The process took 40 minutes to complete 120 cycles. The depth of the etch is checked using a microscope.

Photoresist removal

Photoresist is stripped off from a wafer using a Matrix machine.

Dicing

Dicing is used to cut the wafer and separate out the four different samples(Fig. 5.12). The wafer is attached to a plastic film before starting the dicing operation. The plastic film is then supported on a steel rim. Micro Automation's dicing saw is used. After dicing, four samples of micro bearing surfaces with different sizes and geometries are collected in a petri dish. A schematic of the resulting unit cell can be seen in Fig. 5.13.

5.2.3 Results

Measurements of micro-scale bearing samples using LBDMS encountered many problems. In the first approach, the bearing sample was tethered to the rectangular bracket using four small strips of tape. This approach produced the squeeze film lift upon start of the base oscillation. However, after stopping the base oscillation the squeeze film lift did not always return to zero as the weight of the micro-scale bearing sample was supported by the attached four strips. Another method of testing was tried to test the sample. Here, the sample was constrained to translate in horizontal plane. This was achieved by placing small circular posts of tape at the midpoints of each side of the sample so that the circular post

and sample have in total four point contacts. This test method also did not work as the friction between the circular posts and the bearing sample was far more and the squeeze film could not generate. In the last test method, the micro bearing sample was not constrained

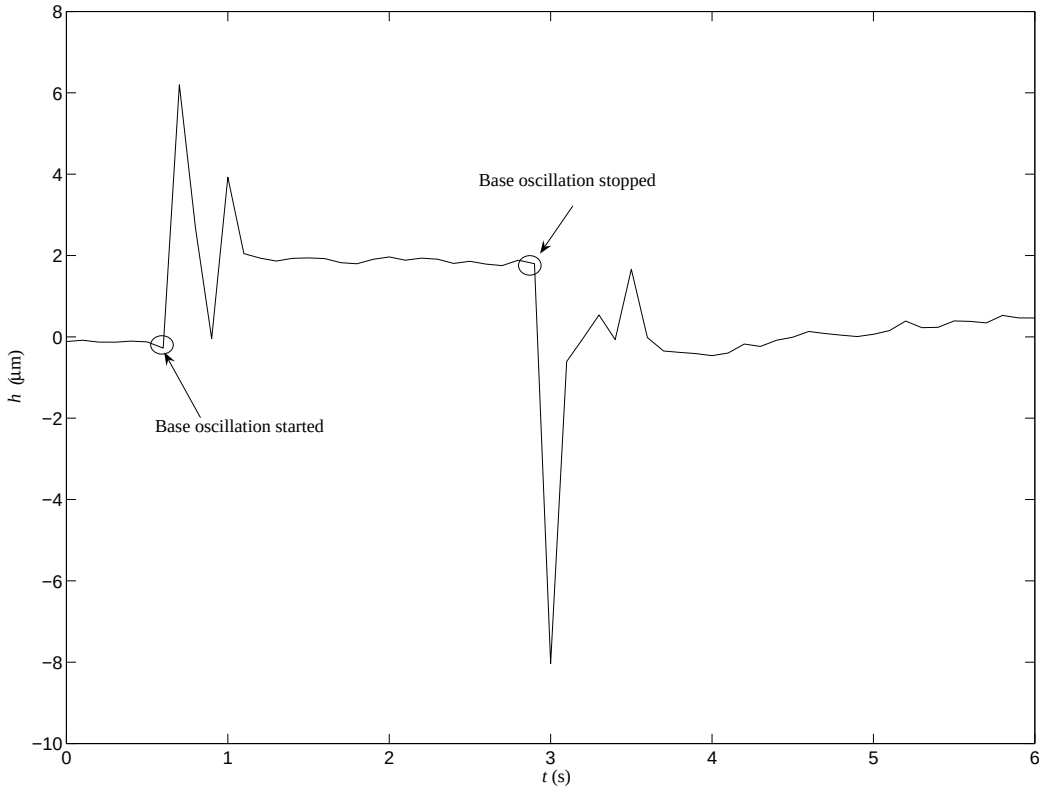

Figure 5.14: Experimental results of micro-scale bearing

by any means. The starting and stopping of base oscillation was performed in approximately 2 seconds. Most of the tests using this method failed because the sample tended to translate in horizontal direction hampering the readings from LBDMS. One good result (See Fig. 5.14) was observed for the bearing configuration d (Fig. 5.13) having diameter of

100 μm and height of 80 μm. Here, once the base oscillation was started, the squeeze film achieved a steady state, and after stopping the base oscillation, it returned to the initial state (Fig. 5.14). For this test case, the frequency of the base oscillation, f, was 2000 Hz

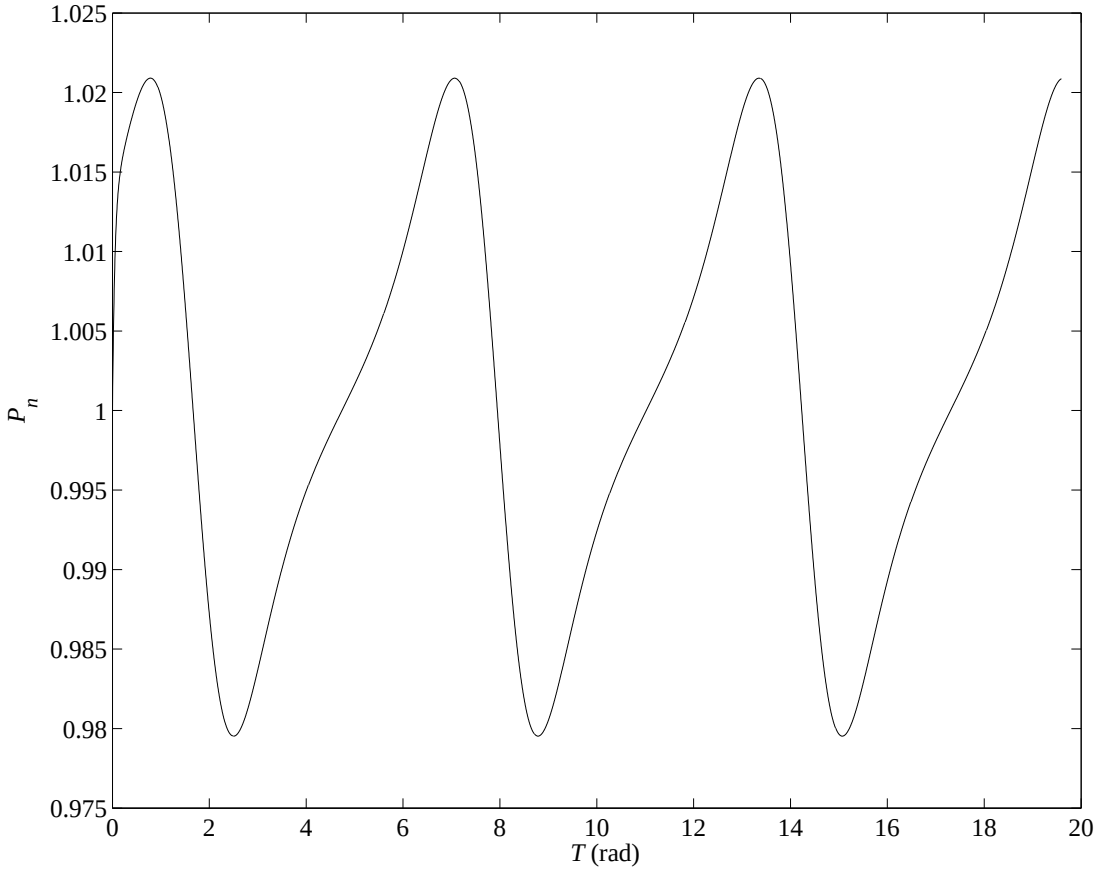

Figure 5.15: Dimensionless mean pressure, P_n, as a function of normalized time, T, for the ultra-thin squeeze film bearing

and the amplitude, Z_0, was 0.63 μm. The mean squeeze film thickness, h_m, obtained was 2 μm. As the weight of the sample is 0.01079 N, the load on one post of bearing surface is

47.955 μN. If the amplitude of oscillation of the squeeze film height is assumed to be 0.63 μm, then the excursion ratio is 0.63/2 (i.e. 0.315). In order to compare the analytical and experimental results, the squeeze film height is assumed as a known function of time (Eq. (5.2)) in analytical work.

$$h = h_m \cdot (1 - \epsilon \cdot sin(T)) \tag{5.2}$$

The Reynolds equation (Eq. (4.22)) is solved for pressure with the assumptions as made in Eq. (5.2) (See Appendix E). The pressure trace obtained is shown in Fig. 5.15. The pressure trace for every cycle is the same. However, the pressure profile is not sinusoidal because of the nonlinear pressure-squeeze film thickness relationship [6] as seen in the governing Reynolds equation (Eq. (4.25)). The mean pressure over one cycle results into a load carrying capacity of 40.16 μN. The % deviation of the theoretical result (from the pressure trace) and the actual load (from weighing the sample) is 16.25. This comparison shows that the experimental results and theoretical results for these micro-scale bearing samples are in good agreement with each other. In future, more comparisons of experimental and simulation results are needed to validate the numerical model.

Chapter 6

Summary

The tribology of macro-scale systems such as power plants, automobiles, air-craft engines etc has been greatly studied in the last century. As the miniaturization of mechanical systems is a need of future technology, it is important to address the issues related to friction, wear and lubrication for such micro-scale mechanical systems. The research undertaken starts with the experimental and analytical study of macro-scale squeeze film bearings which is later extended to study micro-scale squeeze film bearings.

The first part of this research is to extensively study the squeeze film bearings where the squeeze films are characterized as thin films (the film thickness is in the range of 9 to 23 μm). A coupled dynamic model with asperity contact effects is developed to study compressible dynamic squeeze films between disk shaped surfaces, in which, one disk is excited by a sinusoidal displacement. The model presented is general and can be used to investigate dynamic squeeze films with input parameters, frequency (f) and amplitude of vibration (Z_0), mass (m), area of contact (A) and the surface properties. From the results of the numerical simulations, a comparison with F_i and F_n from Salbu's Eq. is made. Based on these comparisons a new semi-analytical equation is developed to predict the load carrying capacity for $0.4 \leq \sigma \leq 10$ using an exponential curve to fit the simulation results. Experimental results disagree quantitatively because of the inability to perfectly model the

experimental system. Qualitatively, the experimental results are in fairly good agreement with the numerical results.

The second part of this research is to study the micro-scale squeeze film bearings, where the squeeze films are characterized as ultra-thin (using Knudsen number, the film thickness should be less than 8 μm). A sample of 3 cm X 3 cm patterned with an array of micro bearing areas having 100 μm diameter is used for an experimental purpose. A single unit cell of this pattern is shown in Fig 5.13. A squeeze film thickness of approximately 2 μm is measured experimentally when the micro bearing was operated at a frequency of 2000 Hz and an amplitude of 0.63 μm. To compare with experimental results, the squeeze film thickness is assumed as a known function of time and the discretized Reynolds equation is solved. The deviation of load carrying capacity from the simulation to the actual load is found to be 16 %. These results are in good agreement with each other, although more extensive work is needed to confirm the results.

In conclusion, numerical simulations and experiments have been performed to investigate the compressible squeeze film bearings. Both experimental and analytical results have shown that the squeeze film bearings have a good potential for lubrication in macro and micro-scale mechanical systems. These results are important in an age where considerable effort has been made to develop gas bearings for MEMS in research laboratories around the world.

Bibliography

[1] Jost, H.P. (2006), Tribology: How a word was coined 40 years ago, in Tribology and Lubrication Technology. pp 24-28.

[2] Kajdas, C., Harvey, S.S.K., and Wilusz, E. (1990), Encyclopedia of Tribology, Elsevier Science Publishing Company Inc., Amsterdam, pp 478.

[3] Hamrock, B.J. (1991), "Fundamentals of Fluid Film Lubrication," NASA Office of Management, Scientific and Technical Information Program: [Supt. of Docs., U.S. G.P.O.,distributor], Washington, D.C., pp 2-9.

[4] Parkins, D.W. and Stanley, W.T. (1982) "Characteristics of an Oil Squeeze Film," J LUBR TECHNOL TRANS ASME, V 104, 4,pp 497-503.

[5] Minikes, A. and Bucher, I. (2003), "Noncontacting lateral transportation using gas squeeze film generated by flexural traveling waves - Numerical analysis" J of the Acoustical Society of America, v 113, 5,pp 2464-2473.

[6] Wiesendanger, M. (2001), "Squeeze film air bearings using piezoelectric bending elements," Ecole Polytechnique Fdrale de Lausanne, Lausanne: EPFL.

[7] Khonsari, M.M. and Booser, E.R. (2001) "Applied tribology : bearing design and lubrication ," John Wiley,New York, pp 258.

[8] Langlois, W.E. (1962), "Isothermal Squeeze Films," Quarterly of Applied Mathematics, 20,2, pp 131-150.

[9] Salbu, E.O.J. (1964), "Compressible squeeze films and squeeze bearings," ASME J. Basic Eng., 86, pp 355-366.

[10] Minikes, A. and Bucher, I. (2003), "Coupled dynamics of a squeeze-film levitated mass and a vibrating piezoelectric disc: Numerical analysis and experimental study," J. Sound Vib., 263, 2, pp 241-268.

[11] Miller, B.A. and Green, I. (2001), "Numerical Formulation for the Dynamic Analysis of Spiral-Grooved Gas Face Seals," ASME J. Tribol., 123, 2, pp 395-403.

[12] Pretlove, A.J. (1985), BASIC mechanical vibrations, Butterworth and Co. (Publishers) Ltd., Kent, England, pp 118.

[13] Griffin, W.S., Richardson, H.H., and Yamanami S. (1966), "A study of Fluid Squeeze-Film Damping," ASME J. Basic Eng., 88, pp 451-456.

[14] Blech, J.J. (1983), "On Isothermal Squeeze Films," J. Lubr. Technol. Trans. ASME, 105, pp 615-620.

[15] Ausman, J.S. (1967) "Gas Squeeze Film Stiffness and Damping Torques on a Circular Disk Oscillating About Its Diameter," J Lubr Technol Trans ASME, 89, pp 219-221.

[16] Etsion, I. (1980), "Squeeze Effects in Radial Face Seals," J Lubr Technol Trans ASME, 102, 2, pp 145-152.

[17] Green, I. and Etsion, I. (1983), "Fluid Film Dynamic Coefficients in Mechanical Face Seals," ASME J. Lubr. Technol., 105, 2, pp 297-302.

[18] Blech, J.J. (1985), "Annular Compressible Squeeze Films," ASME J. Tribol., 107, 4, pp 544-547.

[19] Starr, J.B. (1990), "Squeeze-film damping in solid-state accelerometers," Techn. Digest, Solid State Sensor and Actuator Workshop Hilton Head Island, pp 44-47.

[20] Pan, F., Kubby, J., Peeters, E., Tran, A.T., and Mukherjee, S. (1998), "Squeeze film damping effect on the dynamic response of a MEMS torsion mirror," J. Micromech. Microeng, 8, 3, pp 20-208.

[21] Bao, M., Yang, H., Yin, H., and Sun, Y. (2002), "Energy transfer model for squeeze-film air damping in low vacuum," J. Micromech. Microeng., 12, 3, pp 341-346.

[22] Bao, M., Yang, H., Sun, Y., and French, P.J. (2003), "Modified Reynolds equation and analytical analysis of squeeze-film air damping of perforated structures," J. Micromech. Microeng., 13, 6, pp 795-800.

[23] Nayfeh, A.H. and Younis, M.I. (2004), "A new approach to the modelling and simulation of flexible microstructures under the effect of squeeze film damping," J. Micromech. Microeng, 14, 2, pp 170-181.

[24] Pandey, A.K. and Pratap, R. (2004), "Coupled nonlinear effects of surface roughness and rarefaction on squeeze film damping in MEMS structures," J. Micromech. Microeng, 14, 10, pp 1430-1437.

[25] Same, H. and Wenjing, Y. (2004), "On the squeeze-film damping of micro-resonators in the free-molecule regime," J. Micromech. Microeng., 14, 12, pp 1726-1733.

[26] Zhang, C., Xu, G., and Jiang, Q. (2004), "Characterization of the squeeze film damping effect on the quality factor of a microbeam resonator," J. Micromech. Microeng., 14, 10, pp 1302-1306.

[27] Strawhecker, K., Asay, D. B., McKinney, J., Kim, S. H. (2005), "Reduction of adhesion and friction of silicon oxide surface in the presence of n-propanol vapor in the gas phase," Tribology Letters, 19, 1, pp 17-21.

[28] Epstein, A.H. (2004), "Millimeter-scale, MEMS gas turbine engines," J. Eng. Gas Turbines Power, 126, 2, pp 205-226.

[29] Epstein, A.H., et al. (1997), "Micro-Heat Engines, Gas Turbines, And Rocket Engines -The MIT MICROENGINE PROJECT," American Institute of Aeronautics and Astronautics, pp 1-12.

[30] Breuer, K. (2001), Lubrication in MEMS, Ed. M. Gad el Hak, CRC Press, pp 1-49.

[31] Wong, C.W., Zhang, X., Jacobson, S.A., and Epstein, A.H. (2004), "A Self-Acting Gas Thrust Bearing for High-Speed Microrotors," J Microelectromech Syst, 13, 2, pp 158-164.

[32] Borionettia, G., Bazzali, A., and Orizio, R. (2004), "Atomic force microscopy: a powerful tool for surface defect and morphology inspection in semiconductor industry," Eur. Phys. J. Appl. Phys., 27, pp 101-106.

[33] Sun, Y., Chan, W.K., and Liu, N. (2003), "A slip model with molecular dynamics," J Micromech Microengineering, 12, 3, pp 316-322.

[34] Bird, G.A. (1994), Molecular Gas Dynamics and the Direct Simulation of Gas Flows, Oxford: Clarendon.

[35] Hsia, Y.T. and Domoto, G.A. (1983), "An Experimental Investigation of Molecular Rarefaction Effects in Gas Lubricated Bearings at Ultra Low Clearances," J Lubr Technol Trans ASME, 105, 1, pp 120-130.

[36] Li, W.L. (1999), "Analytical modelling of ultra-thin gas squeeze film," Nanotechnology, 10, pp 440-446.

[37] Darling, R.B., C., H., and J., X. (1997), "Compact analytical modeling of squeeze film damping with arbitrary venting conditions using a Green's function approach," Sens Actuators A Phys, 70, 1-2, pp 32-41.

[38] Veijola, T. and Turowski, M. (2001), "Compact damping models for laterally moving microstructures with gas-rarefaction effects," J Microelectromech Syst, 10, 2, pp 263-273.

[39] Constantinescu, V.N. (1969), Gas Lubrication, The American Society of Mechanical Engineers, New York, USA, pp 621.

[40] Jackson, R.L. and Green, I. (2005), "A Finite Element Study Of Elasto-Plastic Hemisperical Contact Against a Rigid Flat," ASME J. Tribol., 127, 2, pp 343-354.

[41] Jackson, R.L. and Green, I. (2006), "A statistical model of elasto-plastic asperity contact between rough surfaces," Trib. Intl., 39, pp 906-914.

[42] Jaeger, R.C. (1998), Introduction to Microelectronic Fabrication, Prentice Hall, Inc., pp 316.

[43] Greenwood, J.A. and Williamson, J.B.P. (1966), "Contact of Nominally Flat Surfaces," Proc. R. Soc. London, 295, pp 300-319.

[44] McCool, J.I. (1987), "Relating Profile Instrument Measurements to the Functional Performance of Rough Surfaces," ASME J. Tribol., 109, 2, pp 264-270.

[45] Front, I. (1990), "The Effects of Closing Force and Surface Roughness on Leakage in Radial Face Seals," MS Thesis,Technion, Israel Institute of Technology, Israel.

[46] Horton, B.D. (2004), "Magnetic Head Flyability on Patterned Media," MS Thesis, The George W. Woodruff School of Mechanical Engineering, Georgia Institute of Technology, Atlanta, GA.

Appendices

Appendix A

Contact Force

By fitting equations to finite element results, Jackson and Green [40] and [41] provide the following equations to predict the elastic perfectly-plastic contact of a sphere and a rigid flat. ${P^*}_F$ is a ratio of contact load to critical contact load, P_c. For $0 \leq \omega^* \leq {\omega^*}_t$

$$ {P^*}_F = (\omega^*)^{3/2} \tag{A.1} $$

where, ω^* is the ratio of penetration or indentation depth between spherical asperities (ω) to the critical interference (ω_c) and ${\omega^*}_t$ is the value that defines the effective transition from elastic to plastic behavior of ω^*. For Jackson and Green [40], ω^* is 1.9.

For ${\omega^*}_t \leq \omega^*$

$$ {P^*}_F = \left[exp\left(-\frac{1}{4} (\omega^*)^{5/12} \right) \right] (\omega^*)^{3/2} + \frac{4H_G}{CS_y} \left[exp\left(-\frac{1}{25} (\omega^*)^{5/9} \right) \right] (\omega^*) \cdot AE \tag{A.2} $$

where,

$$ \frac{H_G}{S_y} = 2.84 \left[1 - exp\left(-0.82 \left(\frac{\pi C e_y}{2} \sqrt{\omega^*} \left(\frac{\omega^*}{{\omega^*}_t} \right)^{B/2} \right) \right)^{0.7} \right] \tag{A.3} $$

In Eq. (A.3), H_G is the limiting average contact pressure, S_y is yield strength and e_y is uniaxial yield strain (ratio of yield strength to equivalent elastic modulus).

The critical interference to cause initial yielding, ω_c, is derived independently of the hardness, to be

$$\omega_c = \left(\frac{\pi \cdot C \cdot S_y}{2E^{'}}\right)^2 R \tag{A.4}$$

where, R is the radius of the hemispherical asperity and $E^{'}$ is the equivalent elastic modulus. B and C are functions of the material properties given as

$$B = 0.14 \cdot exp\,(23e_y) \tag{A.5}$$

$$C = 1.295 \cdot exp\,(0.736\nu) \tag{A.6}$$

This model then assumes that the individual asperity contact between rough surfaces can be approximated by hemispherical contact with a rigid flat. Then, statistical relationships from Greenwood and Williamson [43] are used to model an entire surface of asperities with a range of heights described by a Gaussian distribution, $G(z)$. These statistical equations are given as

$$F_{cont} = \eta A_n \int_d^\infty \overline{P_F}(z-d)G(z)dz \tag{A.7}$$

where, the average asperity radius of curvature, R, and the asperity surface density, η, are needed to model asperity contact and are obtained from a profilometer produced surface profile using the methods outlined in McCool [44]. The distance between the surfaces can

be described in two ways: (1) the distance between the mean of the surface heights, h, and (2) the distance between the mean of the surface asperities or peaks, d. These values of h and d are related by

$$h = d + y_s \tag{A.8}$$

The value of y_s is derived by Front [45] and given as

$$y_s = \frac{0.045944}{\eta R} \tag{A.9}$$

where, η is the area density of the asperities. Eq. (A.7) is then numerically integrated to predict F_{cont} as a function of h. The surface profile of one of the rough bearing surfaces is used in the work shown in Fig. A.1. Dimensionless contact load for the surface is plotted against dimensionless mean separation (See Fig. A.2). An exponential fit to the data in Fig. A.2 is obtained. The resulting fit, Eq. (A.10) is then included in the numerical simulation to predict the contact force.

$$F_{cont} = \left(-9.98 \cdot \exp\left(-3.621 \cdot \frac{h}{\sigma}\right) + 9.824 \cdot \exp\left(-3.595 \cdot \frac{h}{\sigma}\right)\right) \cdot AE' \tag{A.10}$$

Here, the goodness of fit is

Sum of squares due to error, SSE= 7.586e-008

The ratio of the sum of squares of the regression, R-square= 0.9988

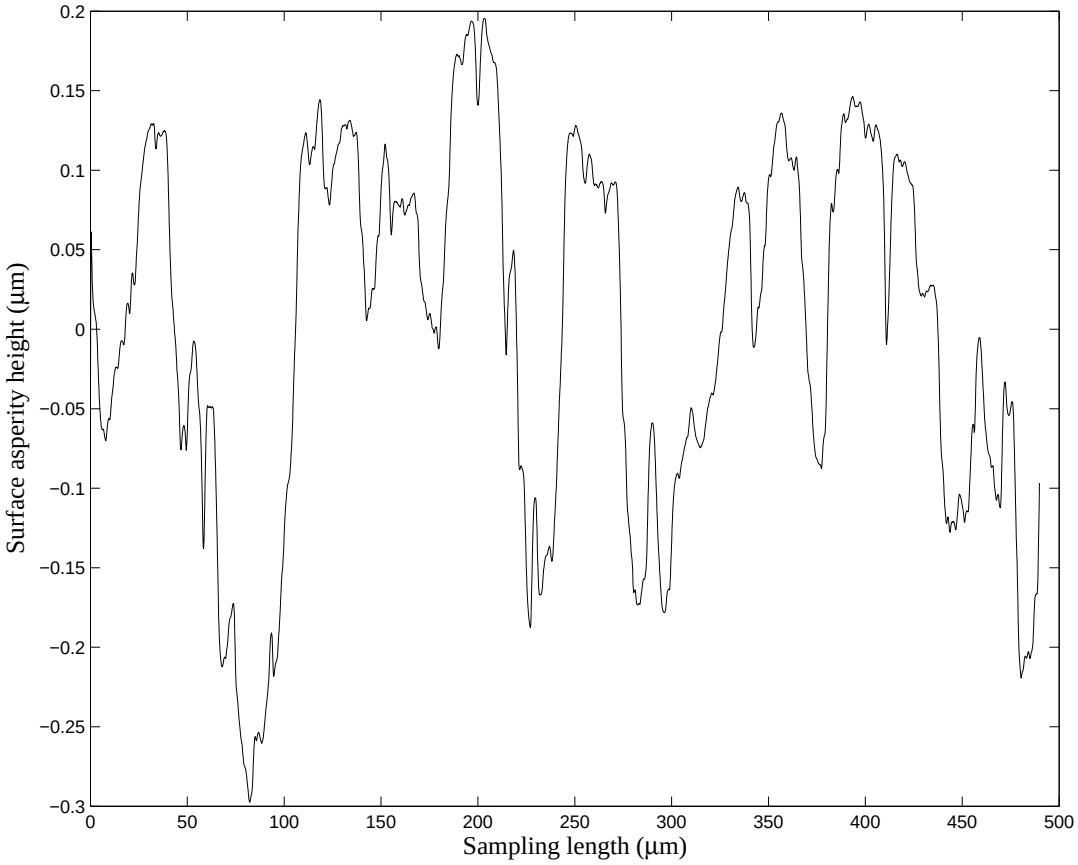

Figure A.1: Surface profile of a rough bearing surface

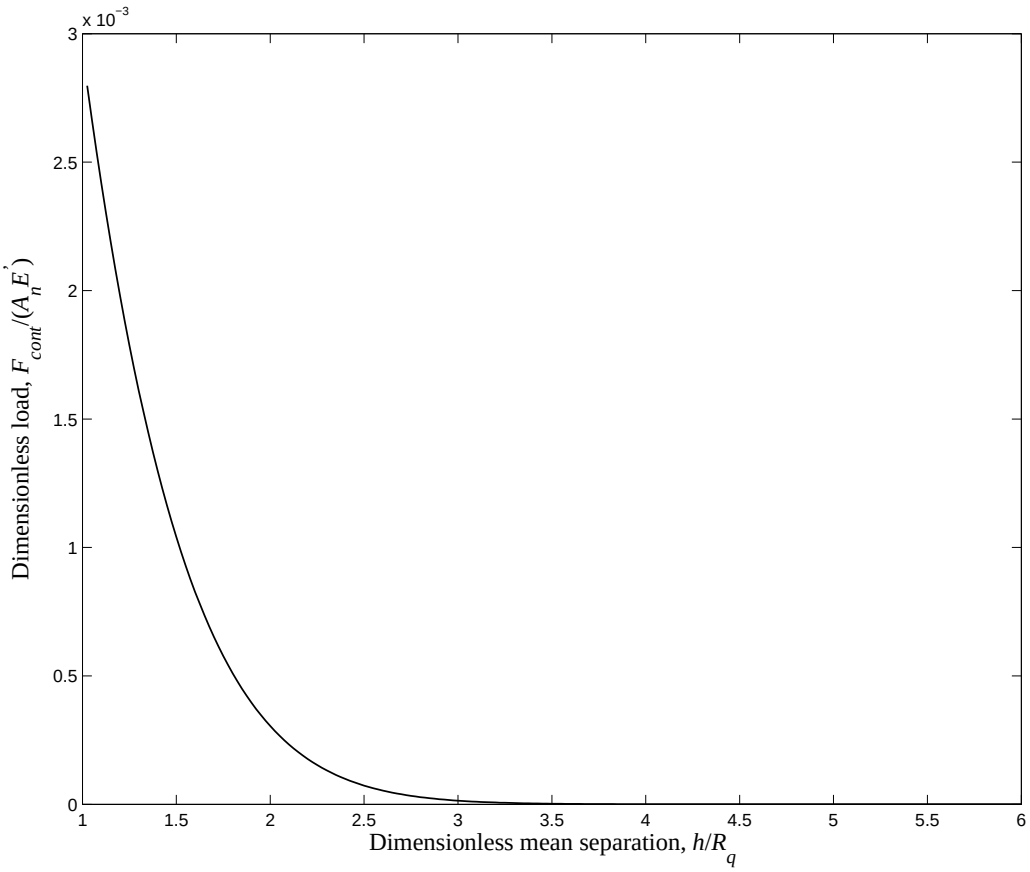

Figure A.2: Dimensionless contact load as a function of dimensionless mean surface separation

Adjusted R-square= 0.9988

Root mean squared error, RMSE= 1.967e-005

Appendix B

C-program to solve the coupled dynamics for thin squeeze films

```
    include <stdio.h>
include <process.h>
include <conio.h>
include <dos.h>
include <math.h>
define MPI 3.14159265358979323 85E0
FILE *f1;
FILE *f2;
FILE *f3;
FILE *f4;
double p[17][2]; // 2-D array for pressure
double meanpressure(double h1,double sigma, double p[][2],double R[],double Rst,double
tst,double h[]);
main()
    /**********************All Variable Declaration************************/
double t; // time
double f; // frquency in Hz
double w; // frequency in radians
double Rst; // Step-size for R
double h[2];
double hdot[2]; // Derivative of Height
double Mult=0; //Dummy variable
double tst; // Time step
double Ro=0; // Radius of circular area (i.e. Area of contact)
double visc; // Vissinity of the oil at T=293
double R[17]; //1-D array for Radius
double Rinv[17];
double pmean=0; //Mean pressure
double pa=0; //atmospheric pressure
double g=9.81; //accn due to gravity
double E=0;
double F=0; //Dummy Variable
double Aml=2.0*pow(10,-6); // Amlitude of the Shaker
double m=7*pow(10,-3);; // Mass of the levitating plate
double Ar; // Area of Contact
```

```
double sig=0.17*pow(10,-6);
double CntFr=0;
double sigma=0;
double YM=0;
double Dum1=0;
double Dum2=0;
double Dum3=0;
double Dum4=0;
double tstDum2=0;
     /********Variables Used for Runge-Kutta********/
double K11=0;
double K12=0;
double K21=0;
double K22=0;
double K31=0;
double K32=0;
double K41=0;
double K42=0;
     /********Variables Used for Runge-Kutta********/
double K1=0;
double K2=0;
double K=0;
double D1=1;
double D2=0;
double D3=0;
double ho=0;
double h1=0;
double hdt=0;
double htst;
double qtst;
double C1=0;
double C2=0;
double C3=0;
double C4=0;
double C5=0;
double x=0;
/****************Assignment of Values********************/
f=1500;
w=2*MPI*f;
visc=1.76/100000;
ho=30*5.554*sig;
Ro=9.0*pow(10,-3);
```

```
pa=101325;
sigma=(12*visc*w*Ro*Ro)/(pa*ho*ho);
Ar=MPI*Ro*Ro;
YM=57.67*pow(10,9); /************Dummy Variables ********************/
Dum1=YM*Ar;
Dum2=1/(w*w*ho);
Dum3=w*w*Aml;
Dum4=(pa/m)*Ar;
     /**********Step Sizes *************/
     Rst=1/16.0;
tst=0.005;
tstDum2=tst*Dum2;
htst=tst/2;
qtst=tst/4; /************ Initial Conditions *****************/
t=0;
h[0]=1;
hdot[0]=0;
pmean=1;
int k=0;
int j=0;
/************ Assignment of Valuesof R @ different node points*******/
R[0]=0;
for(k=0;k<16;k++)
/***************Mean Pressure ***********************/
{
R[k+1]=R[k]+Rst;
}

/***************Assignment of Valuesof R @ Ends Here ***********/
/******Assignment for pressure at time t=0 at all the radius is 1*******/
for(k=0;k<=16;k++)
{
p[k][0]=1;
} /*********Assignment for pressure for initial guess *************/
for(k=0;k<=16;k++)
{
p[k][1]=1;
}
/*******************Assignment of Boundary Conditions ***********/
p[16][1]=1;
// i is for radius //
// and j is for time //
```

```
      x=(h[0]*ho)/sig;
CntFr=(-9.98*exp(-3.621*x)+9.824*exp(-3.595*x))*Dum1;
printf("
f1 = fopen ("Height.txt", "wt"); /****3****/
f2 = fopen ("Hdot", "wt"); /****3****/
f3 = fopen ("MeanPr", "wt"); /****3****/
f4 = fopen ("Time", "wt"); /****3****/
      for (int j=0;j<200000000;j++)
{
      /****************** RK1 ************************/
if(h[0]<2)
{
x=(h[0]*ho)/sig;
CntFr=(-9.98*exp(-3.621*x)+9.824*exp(-3.595*x))*Dum1;
}
else
{ CntFr=0;
}
K11=tst*hdot[0];
K12=tstDum2*(Dum3*sin(t)-0.1*Dum3*sin(7*t)+
(CntFr/m)+(pmean-1)*Dum4-9.810007193613373);
/****************** RK1 ************************/
/**************H and HDOT After RK1**********************/
h1=h[0]+0.5*K11;
hdt=hdot[0]+0.5*K12;
Contact Force
if(h1<2)
{
x=(h1*ho)/sig;
CntFr=(-9.98*exp(-3.621*x)+9.824*exp(-3.595*x))*Dum1; }
else
{
CntFr=0;
}
/******************Mean Pressure **********************/
pmean=meanpressure(h1,sigma,p,R,Rst,htst,h);
/******************RK2*********************************/
t=t+htst;
K21=tst*(hdot[0]+0.5*K12);
K22=tstDum2*(Dum3*sin(t)-0.1*Dum3*sin(7*t)+
(CntFr/m)+(pmean-1)*Dum4- 9.810007193613373);
h1=h[0]+0.5*K21;
```

```
hdt=hdot[0]+0.5*K22;
if(h1<2)
{
x=(h1*ho)/sig;
CntFr=(-9.98*exp(-3.621*x)+9.824*exp(-3.595*x))*Dum1;
}
else
{
CntFr=0;
}
pmean=meanpressure(h1,sigma,p,R,Rst,htst,h);
/******************RK3************************/
K31=tst*(hdot[0]+0.5*K22);
K32=tstDum2*(Dum3*sin(t)-0.1*Dum3*sin(7*t)+
(CntFr/m)+(pmean-1)*Dum4- 9.810007193613373);
/******************RK3************************/
h1=h[0]+K31;
hdt=hdot[0]+K32;
if(h1<2)
{
x=(h1*ho)/sig;
CntFr=(-9.98*exp(-3.621*x)+9.824*exp(-3.595*x))*Dum1;
}
else
{
CntFr=0;
}
pmean=meanpressure(h1,sigma,p,R,Rst,tst,h);
/************RK4*****************/
t=t+htst;
K41=tst*(hdot[0]+K32);
K42=tstDum2*(Dum3*sin(t)-0.1*Dum3*sin(7*t)+
(CntFr/m)+(pmean-1)*Dum4- 9.810007193613373);
h[1]=h[0]+0.16666667*(K11+2*K21+2*K31+K41);
hdot[1]=hdot[0]+0.16666667*(K12+2*K22+2*K32+K42);
/**************Mean Pressure ******************/
h1=h[1];
pmean=meanpressure(h1,sigma,p,R,Rst,tst,h);
      h[0]=h[1];
hdot[0]=hdot[1];
for(int i=0;i<16;i++)
{
```

```
p[i][0]=p[i][1];
}
if(j
{
fprintf(f1,"
fprintf(f2,"
fprintf(f3,"
fprintf(f4,"
}
}
      fclose(f1);
fclose(f2);
fclose(f3);
fclose(f4);
}
      fprintf (f1, "
      double meanpressure(double h1,double sigma, double p[][2],double R[],double Rst,double
tst,double h[])
{
double h3sig,A,B,C,D,R1,R2,P1,P2,pMean;
double error[17];
double M[17];
double err=0;
int s;
h3sig=(pow(h1,3))/(sigma);
B=h1/tst;
      for(s=0;s<=16;s++)
{
M[s]=p[s][1];
}
/****************Assignment of Dummy Variable *****************/
do
{
      for(s=15;s>0;s–)
{ R1=(R[s+1]+R[s])/2;
R2=(R[s-1]+R[s])/2;
A=(h3sig*(R1+R2))/(2*Rst*R[s]);
C=((-p[s][0]*h[0])/tst)-((h3sig)/(2*Rst*R[s]))*
(R1*pow(p[s+1][1],2)+R2*pow(p[s-1][1],2));
p[s][1]=(-B+sqrt(B*B-4*A*C))/(2*A);
if (s==1)
{
```

```
p[0][1]=p[1][1];
}
}
      for(s=15;s>0;s–)
{
D=p[s][1];
p[s][1]=1.1*p[s][1]-0.1*M[s];
error[s]=fabs((p[s][1]-M[s])/p[s][1]);
M[s]=D;
}
p[0][1]=p[1][1];
err=0;
for(s=15;s>0;s–)
{
err=err+error[s];
}
err=err/(15); /// Average error
}
while(err > 0.000001);
P1=0;
P2=0;
for(s=1;s<=15;s=s+2)
{
P1=P1+p[s][1];
}
for(s=2;s<=14;s=s+2)
{
P2=P2+p[s][1];
}
pMean=(p[0][1]+4*P1+2*P2+p[16][1])/48;
return pMean;
}
```

Appendix C

Tables of Experimental and Simulation Results

C.1 Configuration 1

Frequency (Hz)	Amplitude (μm)	Simulation h_m (μm)	Experimental h_m (μm)
800	6.1792	143.2729	0.9447
800	6.669	147.0127	1.2371
800	8.9486	162.775	2.5657
1050	2.4304	6.0489	3.1891
1050	3.617	106.1366	12.0375
1050	4.936	123.2343	21.4303
1050	5.9116	134.5224	23.4826
1300	2.6374	76.4061	6.5227
1300	2.9202	81.0329	7.6587
1300	4.598	107.2562	16.8267

C.2 Configuration 2

Frequency 800 Hz					
Amplitude (μm)	7.4	7.6	7.8	8.0	8.2
Test 1	13.4707	14.269	15.6517	16.274	16.1508
Test 2	13.0979	14.6449	15.0356	15.8266	16.0957
Test 3	13.2905	13.9359	15.6428	15.3388	16.1507
Test 4	13.0951	13.6214	15.0053	15.6878	16.0518
Test 5	13.5354	14.617	14.988	15.7182	16.0818
Test 6	13.9357	15.3383	15.6701	15.6848	16.3287
Test 7	13.445	14.469	15.4086	15.6693	16.0388
Test 8	13.1422	14.3621	15.6795	15.7049	16.5886
Test 9	13.4914	14.8486	15.1449	15.4356	15.8794
Test 10	13.3572	14.8437	15.2333	15.5237	15.508
Average (μm)	13.38611	14.49499	15.34598	15.68637	16.08743
Simulation (μm)	DNC[1]	DNC	DNC	57.3054	60.1417

Frequency 900 Hz					
Amplitude (μm)	5.8	6	6.2	6.4	6.6
Test 1	11.336	11.7322	12.2815	13.0025	13.9145
Test 2	10.6783	11.7956	11.8943	12.5222	13.2427
Test 3	11.01	12.0665	12.23	12.8047	13.263
Test 4	10.8241	11.8172	11.999	12.7467	13.1827
Test 5	11.3899	11.2529	11.8836	13.0562	13.414
Test 6	11.1745	11.6384	12.3865	12.9316	13.8134
Test 7	11.1602	11.7326	12.3004	12.8417	13.5801
Test 8	10.6472	11.1909	12.4745	12.6746	13.4392
Test 9	11.1084	11.1556	12.2482	12.6892	13.2696
Test 10	10.99	11.2763	12.5702	12.896	13.8474
Average (μm)	11.03186	11.56582	12.22682	12.81654	13.49666
Simulation (μm)	DNC	55.5434	58.0158	60.4626	62.4467

[1] DNC -Did Not Converge

Frequency 1000 Hz					
Amplitude (μm)	4.6	4.8	5.0	5.2	5.4
Test 1	11.0867	11.262	11.9811	12.5825	12.6396
Test 2	11.1729	11.1629	12.1185	12.72	12.6326
Test 3	11.264	12.0024	12.2013	12.4823	13.5024
Test 4	10.945	11.9393	12.2688	12.1882	13.1681
Test 5	11.0825	11.485	12.1646	13.0589	12.8527
Test 6	10.958	11.7505	11.9228	12.9179	12.8413
Test 7	10.6522	12.3604	12.3521	12.4905	14.1083
Test 8	10.7868	11.7528	11.8116	12.1864	12.8677
Test 9	11.2518	11.6818	11.8853	12.2711	12.6816
Test 10	10.9668	11.3539	12.1838	11.9896	13.3451
Average (μm)	11.01667	11.6751	12.08899	12.48874	13.06394
Simulation (μm)	DNC	56.4912	59.1097	61.2036	62.9875

Frequency 1500 Hz					
Amplitude (μm)	1.8	2.0	2.2	2.4	2.6
Test 1	9.9339	10.9988	11.0939	11.6938	12.9752
Test 2	10.0439	10.1946	10.8504	12.5324	12.111
Test 3	8.9149	10.3972	10.8781	11.6999	12.7567
Test 4	8.8607	10.5234	10.7668	11.1444	12.5647
Test 5	8.9149	10.9258	11.3802	11.6934	13.2707
Test 6	10.2578	10.9915	11.0566	11.328	12.8714
Test 7	9.9627	10.8179	11.1325	11.9491	12.9994
Test 8	10.0065	10.7677	11.1432	11.8122	12.9973
Test 9	10.0962	10.6744	11.2106	11.8719	11.9577
Test 10	9.9072	10.7097	11.0775	11.5196	12.8166
Average (μm)	9.68987	10.7001	11.05898	11.72447	12.73207
Simulation (μm)	53.5354	56.0012	58.1313	60.0423	61.7946

C.3 Configuration 3

Frequency 800 Hz					
Amplitude (μm)	6.4	6.6	6.8	7.0	7.2
Test 1	21.4024	21.4089	22.1387	22.7954	22.7595
Test 2	20.9746	21.5593	21.8336	22.7572	23.0541
Test 3	21.2554	21.6139	21.7966	22.5867	22.9858
Test 4	20.9251	21.739	21.7729	22.6405	23.2238
Test 5	20.8396	21.7471	22.0179	22.6409	23.1163
Test 6	21.0984	21.4937	21.9323	22.8155	22.9272
Test 7	21.0307	21.4902	21.8789	22.5575	23.0514
Test 8	20.8029	21.438	22.096	22.4713	23.0452
Test 9	20.8746	21.4432	21.7509	22.4318	23.0638
Test 10	20.8737	21.5169	22.0775	22.5943	23.1871
Average (μm)	21.00774	21.54502	21.92953	22.62911	23.04142
Simulation (μm)	65.592	66.6991	67.7418	68.7306	69.6732

Frequency 900 Hz					
Amplitude (μm)	5.2	5.4	5.6	5.8	6.0
Test 1	18.7737	20.1916	20.8962	20.8628	21.7042
Test 2	18.8144	20.0742	21.0646	20.8695	21.5064
Test 3	19.0361	19.9377	20.9214	21.19	21.1382
Test 4	19.1751	19.528	20.9238	21.3347	21.2448
Test 5	19.0633	20.0621	20.9489	21.0129	21.7445
Test 6	18.9867	20.0116	20.8519	21.1412	21.3917
Test 7	19.1702	19.5744	20.4802	21.506	21.196
Test 8	19.0511	19.1967	21.1435	21.0589	21.05
Test 9	19.3148	19.4528	20.7809	20.8976	21.1931
Test 10	19.2281	19.8355	20.9035	21.222	21.3466
Average (μm)	19.06135	19.78646	20.89149	21.10956	21.35155
Simulation (μm)	65.4042	66.5021	67.5448	68.5408	69.4961

Frequency 1000 Hz					
Amplitude (μm)	4	4.2	4.4	4.6	4.8
Test 1	20.8198	22.0756	22.7689	23.0927	23.2616
Test 2	20.1229	22.0891	22.4801	22.8036	23.2182
Test 3	20.3533	21.9974	22.4754	22.8771	23.4326
Test 4	20.5557	22.0531	22.5285	22.5587	22.9707
Test 5	20.887	21.7522	22.322	22.7171	23.0604
Test 6	20.6034	22.1179	22.0915	23.1343	23.7415
Test 7	20.6502	22.0388	22.6978	22.7592	23.4185
Test 8	20.498	21.9899	22.8898	22.4465	23.3308
Test 9	20.6819	22.1545	22.6626	22.5107	23.8755
Test 10	20.8721	21.6264	22.6115	22.9328	23.7882
Average (μm)	20.60443	21.98949	22.55281	22.78327	23.4098
Simulation (μm)	62.8183	64.0531	65.2203	66.331	67.3937

Frequency 1500 Hz					
Amplitude (μm)	1.8	2.0	2.2	2.4	2.6
Test 1	16.2606	16.4348	16.944	17.1475	17.508
Test 2	16.4536	16.7723	16.9895	17.1686	17.2069
Test 3	16.2021	16.406	16.9542	17.2596	17.7354
Test 4	16.3595	16.9441	17.0921	17.2073	17.3995
Test 5	16.4152	16.5749	16.9935	17.4292	17.4173
Test 6	16.145	16.484	16.9261	17.1501	17.5845
Test 7	16.301	16.3783	16.9782	17.3174	17.7091
Test 8	16.2998	16.3724	16.9907	17.02	17.7404
Test 9	16.114	16.678	17.0715	17.2938	17.7186
Test 10	16.1834	16.5505	16.9701	17.2764	17.7282
Average (μm)	16.27342	16.55953	16.99099	17.22699	17.57479
Simulation (μm)	54.5747	56.4424	58.2134	59.8992	61.5094

Appendix D

Calibration of Capacitance Sensor

Equation for calibrating physical capacitance, C to the mean squeeze film thickness, h_m in μm is

$$h_m = \frac{A \cdot \epsilon_0 \cdot k}{1.853 \cdot C^{1.706} + 0.0784} \tag{D.1}$$

where, physical capacitance, C in F is given by

$$C = \omega R_{st} \cdot (-1 + \frac{1}{2.511 \cdot (VR_{exp})^4 + 6.011 \cdot (VR_{exp})^3 - 4.72 \cdot (VR_{exp})^2 + 2.29 \cdot (VR_{exp}) - 0.1417}) \tag{D.2}$$

and

VR_{exp}= experimental voltage ratio as recorded from LabView

ω= frequency of AC voltage, V_{in} (2·π·2000 rad)

R_{st}= resistor used in the electric circuit (33 kΩ)

A= area of contact (m^2)

ϵ_0= permittivity of free space (8.85E-6 F·μm^{-1})

k= dielectric constant of air (1)

Calibration Procedure

1. Read the experimental voltage, $V_{o/p}$ using LabView.

2. Calculate the experimental voltage ratio.

$$VR_{exp} = \frac{\text{Rms } V_{o/p}}{\text{Rms } V_{in}} \tag{D.3}$$

3. Experimental voltage ratio is calibrated in terms of the physical voltage ratio. Standard capacitors are utilized for this calibration. For each standard capacitor, the experimental voltage ratio is calculated. Then, using these standard capacitor values and Eq. (D.5), physical voltage ratios are calculated.

   As,

$$VR_{phys} = \frac{R}{R + \frac{1}{j\omega C}} \tag{D.4}$$

   Thus,

$${VR_{phys}}^2 = \frac{\omega^2 C^2 R^2}{1 + \omega^2 C^2 R^2 + 2\omega RC} \tag{D.5}$$

   Using a curve fitting technique, a polyfit is obtained for VR_{phys} in terms of VR_{exp} and is given by Eq. (D.6). Thus, the experimental voltage ratio is converted to the

physical voltage ratio using the 4^{th} order polynomial (Eq.(D.6)).

$$VR_{phys} = 2.511 \cdot (VR_{exp})^4 + 6.011 \cdot (VR_{exp})^3 - 4.72 \cdot (VR_{exp})^2 + 2.29 \cdot (VR_{exp}) - 0.1417 \quad \text{(D.6)}$$

4. Capacitance due to parallel plate can be calculated using the physical voltage ratio. A quadratic equation in terms of C is written as

$$\left[\left(1 - \frac{1}{{VR_{phys}}^2}\right)\omega^2 {R_{st}}^2\right] C^2 + [2\omega R_{st}]\, C + 1 = 0 \quad \text{(D.7)}$$

Here,

ω=2π·2000 rad

R_{st}=33 kΩ

and VR_{phys} is calculated as per step 3. Solving Eq. (D.7) and taking positive root, C is calculated as

$$C = \omega R_{st} \cdot (-1 + \frac{1}{VR_{phys}}) \quad \text{(D.8)}$$

5. Mylar shims of thickness 38.1 μm are used to calibrate the squeeze film thickness to the capacitance. The two bearing surfaces are separated using mylar shims so that 99.7 percent volume between the two plates is air and 0.3 percent volume is mylar. Thus, two surfaces form two capacitors in parallel, one due to air and the other due

to mylar. Capacitance due to each dielectric medium is calculated using

$$C = \frac{A\epsilon_0 k}{d} \tag{D.9}$$

Here, k for air =1 and k for mylar = 3.2. The total capacitance is the sum of capacitance due to air and mylar. This theoretical capacitance is then calibrated in terms of experimental capacitance (Eq. D.8). This results in a power function which represents the above calibration.

$$C_{cal} = 1.853 \cdot C^{1.706} + 0.0784 \tag{D.10}$$

Here, the goodness of fit is

Variance Reduction= 99.99

S/(N - P) : 0.00002754

RMS (Y - Ycalc) : 0.00262

6. The mean squeeze film height is calculated using Eq. (D.11) as

$$h_m = \frac{A\epsilon_0 k}{C_{cal}} \tag{D.11}$$

Appendix E

Computer program to solve the dynamics for ultra-thin squeeze films

```
    import java.io.*;
import java.math.*;
class Reynoldsequation
{
public static void main(String args[])

{

/*************All Variable Declaration****************/
double Rst; //Step-size for R
double[][] p=new double[17][2]; // 2-D array for pressure
double[] h=new double[2];
double tst; // Time step
double[] R=new double[17]; //1-D array for Radius
double[] M=new double[17];
double[] Rinv=new double[17];
double[] error=new double[17];
double err=0; //Mean pressure
double A=0; //Dummy Variable
double B=0; //Dummy Variable
double C=0; //Dummy Variable
double D=0;
double P1=0; //Dummy Variable
double P2=0; //Dummy Variable
double pmean=1;
double sig=0;
double sig1=0;
double R1=0;
double R2=0;
double K1=0;
double K2=0;
double h3sig;
double visc=1.8*Math.pow(10,-5);
double visc1=0;
double t;
```

```
double N=0;
double Exc=0.315;
int n=0;
double KN=0;
double hm=2*Math.pow(10,-6);
double ME=1.1467*Math.pow(10,-3);


/*************Assignment of Values*********************/
h[0]=1;
sig=929.68;
/**********Step Sizes *************/
tst=0.0001;
/************ Initial Conditions *****************/
t=0;
err=1;
/**************Assignment of Valuesof R @ different node points*********/
R[0]=0;
N=16;
n=16;
Rst=1/N;

for(int k=0;k<N;k++)
{
R[k+1]=R[k]+Rst;
}

/**************Assignment of Valuesof R @ Ends Here ***********/

/*******Assignment for pressure at time t=0 at all the radius is 1*********/
for(int k=0;k<=N;k++)
{
p[k][0]=1;

}
/*********Assignment for pressure for initial guess **************/
for(int k=0;k<=N;k++)
{
p[k][1]=1;
}
/******************Assignment of Boundary Conditions **********/
p[n][1]=1;
```

```
// i is for radius //
// and j is for time //
/******* Finite Difference Algorithm Starts Here***********/
try
{

BufferedWriter out6 = new BufferedWriter (new FileWriter ("Radial.txt"));
BufferedWriter out7 = new BufferedWriter (new FileWriter ("Error.txt"));
BufferedWriter out1 = new BufferedWriter (new FileWriter ("sigma1000R01.txt"));
BufferedWriter out2 = new BufferedWriter (new FileWriter ("sigma1000R051.txt"));
BufferedWriter out3 = new BufferedWriter (new FileWriter ("sigma1000R781.txt"));
BufferedWriter out4 = new BufferedWriter (new FileWriter ("sigma1000R15161.txt"));
BufferedWriter out5 = new BufferedWriter (new FileWriter ("Pressure.txt"));

for (int j=0;j<1600000;j++)
{
/****************** RK1 ************************/
t=t+tst;
h[1]=1-Exc*Math.sin(t);
KN=ME/(h[1]*hm*pmean*101325);
visc1=visc/(1+2*KN+0.2*(Math.pow(KN,0.780))*Math.exp(-KN/10));
sig1=visc1*sig;
h3sig=(Math.pow(h[1],3))/(sig1);
B=h[1]/tst;

/*************Assignment of Dummy Variable ***************/
for(int i=0;i<n;i++)
{
M[i]=p[i][0];
}
p[n][1]=1;

/**************Assignment of Dummy Variable*****************/
do
{
for(int i=15;i>0;i–)
{
R1=(R[i+1]+R[i])/2;
R2=(R[i-1]+R[i])/2;
A=(h3sig*(R1+R2))/(2*Rst*R[i]);
C=((-p[i][0]*h[0])/tst)-((h3sig)/(2*Rst*R[i]))*
(R1*Math.pow(p[i+1][1],2)+R2*Math.pow(p[i-1][1],2));
```

```
p[i][1]=(-B+Math.sqrt(B*B-4*A*C))/(2*A);
if (i==1)
{
p[0][1]=p[1][1];
}
}

for(int i=15;i>0;i–)
{
D=p[i][1];
p[i][1]=1.1*p[i][1]-0.1*M[i];
error[i]=Math.abs((p[i][1]-M[i])/p[i][1]);
M[i]=D;
}
p[0][1]=p[1][1];
err=0;
for(int i=15;i>0;i–)
{
err=err+error[i];

}
err=err/(n-1); /// Average error

}
while(err > 0.0000001);
for(int i=0;i<N;i++)
{
p[i][0]=p[i][1];
}
if(j%200000==0)
{
for(int i=0;i<=N;i++)
{
out6.write(Double.toString(p[i][1]));
out6.newLine();
}
}

P1=0;
P2=0;
for(int i=1;i<=15;i=i+2)
{
```

```
P1=P1+p[i][1];
}
for(int i=2;i<=14;i=i+2)
{
P2=P2+p[i][1];
}
pmean=(p[0][1]+4*P1+2*P2+p[16][1])/48;
if(j%52==0)
{

out5.write(Double.toString(pmean));
out5.newLine();
}
h[0]=h[1];
}
/*******Integration of Pressure using Simpson's Rule Ends Here *********/
out1.close();
out2.close();
out3.close();
out4.close();
out5.close();
out6.close();
out7.close();
}
catch(IOException E2)}}
/******** Finite Difference Algorithm Ends Here***********/
} }
```